

Parameterisation effects in the analysis of AMI Sunyaev–Zel’dovich observations [★]

AMI Consortium: Malak Olamaie,^{1†} Carmen Rodríguez-Gonzálvez,¹
 Matthew L. Davies,¹ Farhan Feroz,¹ Thomas M. O. Franzen,¹ Keith J. B. Grainge,^{1,2}
 Michael P. Hobson,¹ Natasha Hurley-Walker,¹ Anthony N. Lasenby,^{1,2}
 Guy G. Pooley,¹ Richard D. E. Saunders,^{1,2} Anna M. M. Scaife,^{1,3}
 Michel Schammel,¹ Paul F. Scott,¹ Timothy W. Shimwell,¹ David J. Titterton,¹
 Elizabeth M. Waldram,¹ and Jonathan T. L. Zwart^{1,4}

¹ *Astrophysics Group, Cavendish Laboratory, 19 J. J. Thomson Avenue, Cambridge, CB3 0HE*

² *Kavli Institute for Cosmology Cambridge, Madingley Road, Cambridge, CB3 0HA*

³ *Dublin Institute for Advanced Studies, 31 Fitzwilliam Place, Dublin 2, Ireland*

⁴ *Columbia Astrophysics Laboratory, Columbia University, 550 West 120th Street, New York, NY 10027, USA*

Accepted 12/12/11; Received 22/11/10

ABSTRACT

Most Sunyaev–Zel’dovich (SZ) and X-ray analyses of galaxy clusters try to constrain the cluster total mass ($M_T(r)$) and/or gas mass ($M_g(r)$) using parameterised models derived from both simulations and imaging observations, and assumptions of spherical symmetry and hydrostatic equilibrium. By numerically exploring the probability distributions of the cluster parameters given the simulated interferometric SZ data in the context of Bayesian methods, and assuming a β -model for the electron number density $n_e(r)$ described by two shape parameters β and r_c , we investigate the capability of this model and analysis to return the simulated cluster input quantities via three parameterisations. In parameterisation I we assume that the gas temperature is an independent free parameter and assume hydrostatic equilibrium, spherical geometry and an ideal gas equation of state. We find that parameterisation I can hardly constrain the cluster parameters and fails to recover the true values of the simulated cluster. In particular it overestimates $M_T(r_{200})$ and $T_g(r_{200})$ ($M_T(r_{200}) = (6.43 \pm 5.43) \times 10^{15} M_\odot$ and $T_g(r_{200}) = (10.61 \pm 5.28) \text{ keV}$) compared to the corresponding values of the simulated cluster ($M_T(r_{200}) = 5.83 \times 10^{14} M_\odot$ and $T_g(r_{200}) = 5 \text{ keV}$). We then investigate parameterisations II and III in which $f_g(r_{200})$ replaces temperature as a main variable; we do this because f_g may vary significantly less from cluster to cluster than temperature. In parameterisation II we relate $M_T(r_{200})$ and T_g assuming hydrostatic equilibrium. We find that parameterisation II can constrain the cluster physical parameters but the temperature estimate is biased low ($M_T(r_{200}) = (6.8 \pm 2.1) \times 10^{14} M_\odot$ and $T_g(r_{200}) = (3.0 \pm 1.2) \text{ keV}$). In parameterisation III, the virial theorem (plus the assumption that all the kinetic energy of the cluster is the internal energy of the gas) replaces the hydrostatic equilibrium assumption because we consider it more robust both in theory and in practice. We find that parameterisation III results in unbiased estimates of the cluster properties ($M_T(r_{200}) = (4.68 \pm 1.56) \times 10^{14} M_\odot$ and $T_g(r_{200}) = (4.3 \pm 0.9) \text{ keV}$). We generate a second simulated cluster using a generalised NFW (GNFW) pressure profile and analyse it with an entropy based model to take into account the temperature gradient in our analysis and improve the cluster gas density distribution. This model also constrains the cluster physical parameters and the results show a radial decline in the gas temperature as expected. The mean cluster total mass estimates are also within 1σ from the simulated cluster true values: $M_T(r_{200}) = (5.9 \pm 3.4) \times 10^{14} M_\odot$ and $T_g(r_{200}) = (7.4 \pm 2.6) \text{ keV}$ using parameterisation II and $M_T(r_{200}) = (8.0 \pm 5.6) \times 10^{14} M_\odot$ and $T_g(r_{200}) = (5.98 \pm 2.43) \text{ keV}$ using parameterisation III. However, we find that for at least interferometric SZ analysis in practice at the present time, there is no differences in the AMI visibilities between the two models. This may of course change as the instruments improve.

Key words: galaxies: clusters: general – cosmic microwave background – cosmology: observations – methods: data analysis

[★] We request that any reference to this paper cites “AMI Consortium: Olamaie et al. 2011”

[†] Email: mo323@mrao.cam.ac.uk

1 INTRODUCTION

Clusters of galaxies contain large reservoirs of hot, ionized gas. This plasma, although invisible in the optical waveband, can be observed in both X-ray and microwave bands of the electromagnetic spectrum through thermal Bremsstrahlung radiation and its scattering of the cosmic microwave background (CMB) respectively. This inverse Compton scattering results in a decrement in the intensity of CMB photons in the direction of the cluster at frequencies < 218 GHz, and is known as the Sunyaev–Zel’dovich (SZ) effect (Sunyaev & Zeldovich 1970; Birkinshaw 1999; Carlstrom, Holder, & Reese 2002). To describe the full spectral behaviour of the SZ effect, one needs to consider three main components. These include the thermal SZ effect caused by thermal (random) motion of scattering electrons, including thermal weakly relativistic electrons, the kinematic SZ effect caused by peculiar velocity of the cluster with respect to Hubble flow, and relativistic effects caused by presence of the energetic nonthermal electrons in the hot plasma of the cluster that are responsible for synchrotron emission of radio halos or relics. However, since the last two processes have significantly smaller effects on the overall spectral distortion at cm wavelengths, we only consider the thermal SZ effect in this paper. Moreover, we ignore the effects of weakly relativistic thermal electrons, which are negligible at cm wavelengths.

A main science driver for studying clusters through their thermal SZ signal arises from the fact that SZ surface brightness is independent of redshift. This provides us with a powerful opportunity to study galaxy clusters out to high redshift. However, estimating the physical properties of the clusters depends strongly on the model assumptions. In this paper we aim to show how employing different parameterisations for a cluster model affects the constraints on cluster properties. These tasks are conveniently carried out through Bayesian inference using a highly efficient parameter space sampling method: nested sampling (Skilling 2004). This sampling method is employed using the package MULTINEST (Feroz & Hobson 2008; Feroz, Hobson & Bridges 2009). MULTINEST explores the high dimensional parameter space and calculates both the probability distribution of cluster parameters and the Bayesian evidence. This algorithm is employed to analyse real multi-frequency SZ observations made by the Arcminute Microkelvin Imager (AMI), (AMI Consortium: Zwart et al. 2008).

The rest of the paper is organised as follows. In Section 2, we describe the AMI telescope. In Section 3, we discuss Bayesian inference. Section 4 gives details of how we model interferometric SZ data. In Section 5, we describe the modelling of the SZ signal using both the isothermal β -model and an “entropy”-GNFW pressure model. Section 6 outlines the assumptions needed to estimate cluster physical parameters and describes how different parameterisations introduce different constraints and biases in the resulting marginalised posterior probability distributions. In Section 7, we describe how to generate a simulated SZ cluster in a consistent manner for both models, and in Section 8, we present our results. Finally, Section 9 summarises our conclusions.

2 THE ARCMINUTE MICROKELVIN IMAGER (AMI)

AMI comprises two arrays: the Small Array (SA) and the Large Array (LA) located at the Mullard Radio Astronomy Observatory near Cambridge. The SA consists of ten 3.7-m diameter equatorially-mounted antennas surrounded by an aluminium groundshield to suppress ground-based interference and to ensure that the sidelobes

Table 1. AMI technical summary.

	SA	LA
Antenna Diameter	3.7 m	12.8 m
Number of Antennas	10	8
Baseline Lengths (current)	5–20 m	18–110 m
Primary Beam at 15.7 GHz	20′1	5′5
Synthesized Beam	$\approx 3'$	$\approx 30''$
Flux Sensitivity	30 mJy s ^{-1/2}	3 mJy s ^{-1/2}
Observing Frequency	13.5–18 GHz	13.5–18 GHz
Bandwidth	3.7 GHz	3.7 GHz
Number of Channels	6	6
Channel Bandwidth	0.75 GHz	0.75 GHz

from the antennas do not terminate on warm emitting material. The LA consists of eight 13-m diameter antennas. A summary of the technical details of AMI is given in Table 1. Further details of the instrument are in AMI Consortium: Zwart et al. (2008).

3 BAYESIAN INFERENCE

Bayesian inference has been shown to provide an efficient and robust approach to parameter estimation in astrophysics and cosmology by offering consistent procedures for the estimation of a set of parameters Θ within a model (or hypothesis) H using the data \mathbf{D} without loss of information. Bayes’ theorem states that:

$$Pr(\Theta|\mathbf{D}, H) = \frac{Pr(\mathbf{D}|\Theta, H) Pr(\Theta|H)}{Pr(\mathbf{D}|H)}, \quad (1)$$

where $Pr(\Theta|\mathbf{D}, H) \equiv P(\Theta)$ is the posterior probability distribution of the parameters, $Pr(\mathbf{D}|\Theta, H) \equiv \mathcal{L}(\Theta)$ is the likelihood, $Pr(\Theta|H) \equiv \pi(\Theta)$ is the prior probability distribution and $Pr(\mathbf{D}|H) \equiv \mathcal{Z}$ is the Bayesian evidence.

Bayesian inference in practice often divides into two parts: parameter estimation and model selection. In parameter estimation, the normalising evidence factor is usually ignored, since it is independent of the parameters Θ , and inferences are obtained by taking samples from the unnormalised posterior distributions using sampling techniques. The posterior distribution can be subsequently marginalised over each parameter to give individual parameter constraints.

In contrast to parameter estimation, for model selection the evidence takes the central role and is simply the factor required to normalise the posterior over Θ :

$$\mathcal{Z} = \int \mathcal{L}(\Theta)\pi(\Theta)d^D\Theta, \quad (2)$$

where D is the dimensionality of the parameter space. The question of model selection between two models H_0 and H_1 is then decided by comparing their respective posterior probabilities, given the observed data set \mathbf{D} , via the model selection ratio

$$R = \frac{Pr(H_1|\mathbf{D})}{Pr(H_0|\mathbf{D})} = \frac{Pr(\mathbf{D}|H_1) Pr(H_1)}{Pr(\mathbf{D}|H_0) Pr(H_0)} = \frac{\mathcal{Z}_1 Pr(H_1)}{\mathcal{Z}_0 Pr(H_0)}, \quad (3)$$

where $Pr(H_1)/Pr(H_0)$ is the *a priori* probability ratio for the two models. It should be noted that the evaluation of the multidimensional integral in the Bayesian evidence is a challenging numerical task which can be tackled by using MULTINEST. This Monte-Carlo method is targeted at the efficient calculation of the evidence, but also produces posterior inferences as a by-product. This method

is also very efficient in sampling from posteriors that may contain multiple modes or large (curving) degeneracies.

4 MODELLING INTERFEROMETRIC SZ DATA

In the cluster plasma the central optical depth τ is typically between 0.001–0.01 and the temperature T varies from 10^7 – 10^8 K. Thus the observed SZ surface brightness in the direction of electron reservoir may be described as

$$\delta I_\nu = T_{\text{CMB}} y f(\nu) \left. \frac{\partial B_\nu}{\partial T} \right|_{T=T_{\text{CMB}}} \quad (4)$$

Here B_ν is the blackbody spectrum, $T_{\text{CMB}} = 2.73$ K (Fixsen et al. 1996) is the temperature of the CMB radiation, $f(\nu) = \left(x \frac{e^x + 1}{e^x - 1} - 4\right) (1 + \delta(x, T_e))$ is the frequency dependence of thermal SZ signal, $x = \frac{h_p \nu}{k_B T_{\text{CMB}}}$, h_p is Planck's constant, ν is the frequency and k_B is Boltzmann's constant. $\delta(x, T_e)$ takes into account the relativistic corrections in the study of the thermal SZ effect which is due to the presence of thermal weakly relativistic electrons in the ICM and is derived by solving the Kompaneets equation up to the higher orders (Rephaeli 1995, Itoh et al. 1998, Nozawa et al. 1998, Pointecouteau et al. 1998 and Challinor and Lasenby 1998). It should be noted that at 15 GHz (AMI observing frequency) $x = 0.3$ and therefore the relativistic correction, as shown by Rephaeli (1995), is negligible for $k_B T_e \leq 15$ keV. The dimensionless parameter y , known as Comptonisation parameter, is the integral of the number of collisions multiplied by the mean fractional energy change of photons per collision, along the line of sight

$$y = \frac{\sigma_T}{m_e c^2} \int_{-\infty}^{+\infty} n_e(r) k_B T_e(r) dl \quad (5)$$

$$= \frac{\sigma_T}{m_e c^2} \int_{-\infty}^{+\infty} P_e(r) dl, \quad (6)$$

where $n_e(r)$, $P_e(r)$ and T_e are the electron number density, pressure and temperature at radius r respectively. σ_T is Thomson scattering cross-section, m_e is the electron mass, c is the speed of light and dl is the line element along the line of sight. It should be noted that in equation (6) we have used the ideal gas equation of state.

An interferometer like AMI operating at a frequency ν measures samples from the complex visibility plane $\tilde{I}_\nu(\mathbf{u})$. These are given by a weighted Fourier transform of the surface brightness $I_\nu(\mathbf{x})$, namely

$$\tilde{I}_\nu(\mathbf{u}) = \int A_\nu(\mathbf{x}) I_\nu(\mathbf{x}) \exp(2\pi i \mathbf{u} \cdot \mathbf{x}) d\mathbf{x}, \quad (7)$$

where \mathbf{x} is the position relative to the phase centre, $A_\nu(\mathbf{x})$ is the (power) primary beam of the antennas at observing frequency ν (normalised to unity at its peak) and \mathbf{u} is the baseline vector in units of wavelength. In our model, the measured visibilities are defined as

$$V_\nu(\mathbf{u}) = \tilde{S}_\nu(\mathbf{u}) + N_\nu(\mathbf{u}), \quad (8)$$

where the signal component, $\tilde{S}_\nu(\mathbf{u})$, contains the contributions from the SZ cluster and identified radio point sources whereas the generalised noise part, $N_\nu(\mathbf{u})$, contains contributions from background of unsubtracted radio point sources, primary CMB anisotropies and instrumental noise.

We assume a Gaussian distribution for the generalised noise. This component then defines the likelihood function for the data

$$\mathcal{L}(\Theta) = \frac{1}{Z_N} \exp\left(-\frac{1}{2} \chi^2\right), \quad (9)$$

where χ^2 is the standard statistic quantifying the misfit between the observed data \mathbf{D} and the predicted data $\mathbf{D}^p(\Theta)$:

$$\chi^2 = \sum_{\nu, \nu'} (\mathbf{D}_\nu - \mathbf{D}_\nu^p)^T (\mathbf{C}_{\nu, \nu'})^{-1} (\mathbf{D}_{\nu'} - \mathbf{D}_{\nu'}^p), \quad (10)$$

where ν and ν' are channel frequencies. \mathbf{C} is the generalised noise covariance matrix

$$\mathbf{C} = \mathbf{C}_{\nu, \nu'}^{\text{rec}} + \mathbf{C}_{\nu, \nu'}^{\text{CMB}} + \mathbf{C}_{\nu, \nu'}^{\text{conf}}, \quad (11)$$

and the normalisation factor Z_N is given by

$$Z_N = (2\pi)^{(2N_{\text{vis}})/2} |\mathbf{C}|^{1/2}, \quad (12)$$

where N_{vis} is the total number of visibilities. It should be noted that since the main goal of this paper is to demonstrate the effect of different parameterisations in modelling the SZ cluster signal, we ignore the contributions due to subtracted and unsubtracted radio point sources so that the non-Gaussian nature of these sources is irrelevant. Moreover, the simulations, used in our analysis do not include extragalactic radio sources or diffuse foreground emission from the galaxy. The effects of the former have already been addressed in Feroz et al. (2009), and here we wish to concentrate on the different parameterisation of the cluster. We also note that foreground galactic emission is unlikely to be a major contaminant since our interferometric observations resolve out large-scale emission.

5 ANALYSING THE SZ SIGNAL: β -MODEL VERSUS GNFV MODEL

As may be seen from equations (5) and (6), in order to calculate the y parameter and therefore to model the SZ signal, we need to assume either density and temperature profiles (Feroz et al. 2009; AMI Consortium: Zwart et al. 2010; AMI Consortium: Rodríguez-González et al. 2011) or a pressure profile (Nagai et al. 2007; Mroczkowski et al. 2009; Arnaud et al. 2010; Plagge et al. 2010 and Planck Collaboration 2011d) for the plasma content of the galaxy cluster. It is also possible to assume a profile for the gas ‘‘entropy’’ and then derive the distribution of gas pressure assuming hydrostatic equilibrium (Allison et al. 2011). Indeed, in general, one may choose to model the SZ signal by assuming parameterised functional forms for any two linearly independent functions of the ICM thermodynamic quantities.

Following our previous analysis methodology (Feroz et al. 2009; AMI Consortium: Zwart et al. 2010; AMI Consortium: Rodríguez-González et al. 2011), we first review the application of the isothermal β -model in modelling the SZ effect and extracting the cluster physical parameters demonstrating the impact of different parameterisations on the inferred cluster properties within a model. We then repeat our analysis for the Generalised NFW (GNFW) pressure profile, first presented in Nagai et al. (2007), together with the entropy profile presented in Allison et al. (2011) to model the SZ effect and derive the cluster physical parameters. This approach has potential advantages. It not only removes the assumption of isothermality but also leads to a density profile that is more consistent with the results of the both numerical analysis of hydrodynamical simulations (Voit et al. 2003; Nagai et al. 2006; Kravtsov 2006; Hallman et al. 2007) and deep X-ray observations of galaxy clusters (Pratt & Arnaud 2002; Vikhlinin et al. 2006).

5.1 Isothermal β -model

This model assumes a β -profile for electron number density (Cavaliere and Fusco-Femiano 1976, 1978) and a constant temperature throughout the cluster

$$n_e(r) = \frac{n_e(0)}{\left(1 + \frac{r^2}{r_c^2}\right)^{3\beta/2}},$$

$$T_e(r) = T_g(r) = \text{constant.} \quad (13)$$

Here $n_e(0)$ is the central electron number density, T_e is the electron temperature, which is assumed to be the same as the gas temperature, T_g , and r_c is the core radius. It should be noted that in our model, β is considered as a free fitting parameter (Plagge et al. 2010; AMI Consortium: Zwart et al. 2010) and is not fixed to for example: $\langle\beta_{\text{fit}}\rangle = 2/3$ (Sarazin 1988).

Using this isothermal β -model, we can then calculate a map of the y parameter on the sky along the line of sight by solving the integral in equation (5) analytically (Birkinshaw et al. 1999)

$$y(s) = y_0 \left(1 + \frac{s^2}{r_c^2}\right)^{(1-3\beta)/2}, \quad (14)$$

where $\beta > 1/3$, s is the projected distance from the centre of the cluster on the sky such that $r^2 = s^2 + l^2$ and y_0 is the central Comptonisation parameter

$$y_0 = \frac{\sqrt{\pi}\sigma_T k_B T_g n_e(0) r_c \Gamma(\frac{3\beta}{2} - \frac{1}{2})}{m_e c^2 \Gamma(\frac{3\beta}{2})}. \quad (15)$$

The integral of the y parameter over the solid angle Ω subtended by the cluster is denoted by Y_{SZ} , and is proportional to the volume integral of the gas pressure. It is thus a good estimate for the total thermal energy content of the cluster and its mass (see e.g. Bartlett & Silk 1994). Thus determining the normalisation and the slope of $Y_{\text{SZ}} - M$ relation have been the subject of studies of the SZ effect (da Silva et al. 2004; Nagai 2006; Kravtsov 2006; Plagge et al. 2010; Andersson et al. 2011; Arnaud et al. 2010; Planck Collaboration 2011d,e,f,g,h). In particular, Andersson et al. (2011) investigated the $Y_{\text{SZ}} - Y_X$ scaling relation within a sample of 15 clusters observed by South Pole Telescope (SPT), Chandra and XMM-Newton and found a slope of close to unity (0.96 ± 0.18). Similar studies were carried out by Planck Collaboration (Planck Collaboration 2011g) using a sample of 62 nearby ($z < 0.5$) clusters observed by both Planck and XMM-Newton satellites. The results are consistent with predictions from X-ray studies (Arnaud et al. 2010) and the ones presented in Andersson et al. (2011). These studies at low redshifts where the data are available from both X-ray and SZ observations of galaxy clusters are crucial to calibrate the $Y_{\text{SZ}} - M$ relation and such a relation can then be scaled and used to determine masses of SZ selected clusters at high redshifts in order to constrain cosmology.

We calculate the Y_{SZ} parameter for the isothermal β -model in both cylindrical and spherical geometries. Assuming azimuthal symmetry, Y_{cyl} reads

$$Y_{\text{cyl}}(R) = \frac{\sigma_T}{m_e c^2} \int_{-\infty}^{+\infty} dl \int_0^R P_e(r) 2\pi s ds \quad (16)$$

$$= \int_0^R y(s) 2\pi s ds \quad (17)$$

$$= \begin{cases} \frac{\pi y_0 r_c^2}{\frac{3}{2} - \frac{3\beta}{2}} \left\{ \left(1 + (R/r_c)^2\right)^{(3-3\beta)/2} - 1 \right\} & \beta \neq 1 \\ \pi y_0 r_c^2 \ln[1 + (R/r_c)^2] & \beta = 1, \end{cases}$$

where R is the projected radius of the cluster on the sky.

The integrated y parameter in the case of assuming spherical geometry Y_{sph} , is given by integrating the plasma pressure within a spherical volume of radius r

$$Y_{\text{sph}}(r) = \frac{\sigma_T}{m_e c^2} \int_0^r P_e(r') 4\pi r'^2 dr' \quad (18)$$

$$= \frac{\sigma_T k_B T_g n_e(0)}{m_e c^2} \int_0^r \frac{4\pi r'^2 dr'}{\left(1 + \frac{r'^2}{r_c^2}\right)^{3\beta/2}}. \quad (19)$$

It should be noted that there is an analytical solution for the above integral provided that the upper limit is infinity and $\beta > 1$. However, since we study the cluster to a finite extent and β varies over a wide range including $\beta < 1$, we calculate Y_{sph} numerically.

5.2 GNFW Pressure Profile

As the SZ surface brightness is proportional to the line of sight integral of the electron pressure, assuming a pressure profile for the hot plasma within the cluster to model the SZ effect seems a reasonable choice. In this context, Nagai et al. (2007) analysed the pressure profiles of a series of simulated clusters (Kravtsov et al. 2005) as well as a sample of relaxed real clusters presented in Vikhlinin et al. (2005, 2006). They found that the pressure profiles of all of these clusters can be described by a generalisation of the Navarro, Frenk, and White (Navarro et al. 1997) (NFW) model used to describe the dark matter halos of simulated clusters. The GNFW pressure profile (Nagai et al. 2007) is described as

$$P_e(r) = \frac{P_{\text{ei}}}{\left(\frac{r}{r_p}\right)^c \left(1 + \left(\frac{r}{r_p}\right)^a\right)^{(b-c)/a}}, \quad (20)$$

where P_{ei} is the normalisation coefficient of the pressure profile, r_p is the scale radius and the parameters (a, b, c) describe the slopes of the pressure profile at $r \approx r_p$, $r > r_p$ and $r \ll r_p$ respectively. We fix the values for the slopes to the ones given in Arnaud et al. (2010): $(a, b, c) = (1.0620, 5.4807, 0.3292)$. Arnaud et al. (2010) derived the pressure profiles for the REXCESS cluster sample from XMM-Newton observations (Böhringer et al. 2007; Pratt et al. 2010 and Arnaud et al. 2010) within r_{500} . These pressure profiles also match (within r_{500}) three sets of different numerical simulations (Borgani et al. 2004; Piffaretti & Valdarni 2008; Nagai et al. 2007). They thus derived an analytical function, the so-called universal pressure profile with above mentioned parameters. This profile has been successfully tested against SZ data from SPT (Plagge et al. 2010) and the Planck survey data (Planck Collaboration 2011d).

We calculate the map of the y parameter on the sky along the line of sight by solving the integral in equation (6) numerically. However, we note that the central Comptonisation parameter y_0 has an analytical solution

$$y_0 = \frac{2\sigma_T P_{\text{ei}} r_p}{m_e c^2} \frac{1}{a} \frac{\Gamma(\frac{1-c}{a}) \Gamma(\frac{b-1}{a})}{\Gamma(\frac{b-c}{a})}. \quad (21)$$

Similarly, to calculate the thermal energy content of the cluster within a sphere with finite radius we use equation (18). In this context, Arnaud et al. (2010) have shown that the pressure profile flattens at the radius of $5r_{500}$ and used this to define the boundary of the cluster. One can thus use this radius to define the total volume integrated SZ signal.

$$Y_{\text{tot}} = Y_{5r_{500}} = \frac{\sigma_T}{m_e c^2} \int_0^{5r_{500}} P_e(r') 4\pi r'^2 dr' \quad (22)$$

6 ESTIMATING CLUSTER PHYSICAL PARAMETERS

To study the physical parameters of the cluster, such as its total mass and gas mass, we have to make some assumptions about the dynamical state of the cluster. The most widely-used assumptions are: that the gas distribution is in hydrostatic equilibrium with the cluster total gravitational potential dominated by dark matter, and that both dark matter and the plasma are spherically symmetric and have the same centroid.

The cluster mass $M_T(r_X)$ is also defined as the total amount of matter internal to radius r_X within which the mean density of the cluster is X times the critical density at the cluster redshift. Mathematically, the assumption of hydrostatic equilibrium applies everywhere inside the cluster and relates total cluster mass internal to radius r to the gas pressure gradient at that radius and hence to the density and temperature gradients respectively

$$M_T(r) = -\frac{k_B T_g(r)r}{\mu G} \left[\frac{d \ln \rho_g(r)}{d \ln r} + \frac{d \ln T_g(r)}{d \ln r} \right], \quad (23)$$

where $\mu = 0.6m_p$ (Sarazin 1988) is the mean mass per gas particle, m_p is the proton mass and G is the universal gravitational constant. Assuming spherical geometry, it is also possible to calculate the gas mass and total mass internal to radius r_X

$$M_g(r_X) = 4\pi \int_0^{r_X} r^2 \rho_g(r) dr, \quad (24)$$

$$M_T(r_X) = \frac{4\pi}{3} r_X^3 (X \rho_{\text{crit}}(z)). \quad (25)$$

Here $\rho_{\text{crit}}(z) = \frac{3H(z)^2}{8\pi G}$ is the critical density of the universe at the cluster redshift z and $H(z) = H_0 \sqrt{(\Omega_M + \Omega_\Lambda Q)(1+z)^3 + \Omega_R(1+z)^4 + \Omega_K(1+z)^2}$ is the Hubble parameter at redshift z , where $H_0 = 100h \text{ km s}^{-1} \text{ Mpc}^{-1}$ is the Hubble constant now. Ω_M measures the present mean mass density including baryonic and nonbaryonic dark matter in non-relativistic regime, Ω_Λ takes into account the present value of the dark energy, Ω_R measures the current energy density in the CMB and the low mass neutrinos, Ω_K describes the curvature of the universe and $Q = (1+z)^{3(w_0+w_a)} \exp\left[\frac{-3w_a z}{1+z}\right]$ is the dark energy equation of state.

Moreover, it has been long known that the total mass of the cluster is strongly correlated with its mean temperature. This arises from both X-ray observations of galaxy clusters (Voit & Ponman 2003) and the fact that the gravitational heating is the dominant process in the clusters within the hierarchical structure formation scenario (Kaiser 1986 ; Sarazin 2008).

Assuming virialisation and that all cluster kinetic energy is in gas internal energy suggests that $T \propto M^{2/3}$, where T is the mean gas temperature within the virial radius and M is the cluster total mass internal to that radius. However, an extensive range of studies based both on observations of galaxy clusters and on numerical simulations have been carried out aiming to determine the proportionality coefficient of such relation (Evrard et al. 1996; Eke et al. 1998; Voit 2000; Yoshikawa et al. 2000; Finoguenov et al. 2001; Afshordi & Renyue 2002; Evrard et al. 2002; Sanderson et al. 2003; Borgani et al. 2004; Voit 2005; Arnaud et al. 2005; Vikhlinin et al. 2006; Afshordi et al. 2007; Maughan et al. 2007 and Nagai et al. 2007). Finoguenov et al (2001) studied the observational mass-temperature relation of two sets of cluster samples. In their first sample they used the assumption of isothermality whereas in the second set they knew the temperature gradient of the clusters within the sample. In both samples, they found that the discrepancy from the self-similarity in the M-T relation is more pronounced in the low mass clusters ($k_B T_g < 3.5 \text{ keV}$) as non-gravitational

processes become more dominant in these clusters. Similar results were obtained by Arnaud et al. (2005) when they analysed a sample of 10 nearby ($z \leq 0.15$) relaxed clusters in the temperature range 2 – 9 keV. They showed that the slope of the M-T relation for hot clusters is consistent with self-similar expectation while for low temperature (low mass) clusters the slope is significantly higher. Studies of the observational mass- X-ray luminosity relation (Maughan et al. 2007) also show that the scatter in the $L_X - M_{500}$ relation is dominated by cluster cores and is almost insensitive to the merger status of the cluster. Theoretical studies based on the adiabatic simulations and the hydrodynamical simulations of cluster formation with gravitational heating only also verify the slope of 3/2 in M-T relation (Evrard et al. 1996; Eke et al. 1998; Voit 2000; Yoshikawa et al. 2000) while numerical simulations which take into account the non-gravitational heating processes and the effect of the radiative cooling of the gas (Borgani et al. 2004; Nagai et al. 2007) do predict a slightly higher slope. Moreover, almost all of the above mentioned studies do agree that the discrepancy in the slope of the M-T relation could also be due to the different procedures used for estimating masses in simulations and observational analyses.

In this paper we therefore decided to follow the approach given in Voit (2005). This is based on using the virial theorem to relate a collapsing top-hat density perturbation model to a singular truncated isothermal sphere. It also takes into account the finite boundary pressure and assumes all kinetic energy is internal energy of the hot plasma. This gives

$$k_B T_g(r_X) = \frac{\mu}{2} \left(\frac{X}{2} \right)^{1/3} [GM_T(r_X)H(z)]^{2/3}. \quad (26)$$

It should be noted that above relation assumes that the virialisation occurs at r_X .

Based on the above assumptions, one can adopt different parameterisations to study physical properties of the cluster within a particular model (e.g. using either the assumption of hydrostatic equilibrium or the M-T relation). These different approaches shed light on the realism of the assumptions made throughout the analysis and reveal different biases and constraints associated with them. In a single- frequency observation that at least partially resolves the cluster, the best one can hope to achieve in constraining an empirical model of the SZ decrement is to estimate the central position of the cluster (the position of the decrement) and two further parameters—i.e. shape and scale parameters. The interpretation of such constraints does however depend on the particular parameterisation.

Hence in the following sections we discuss different possible parameterisations within two models: isothermal β -model and “entropy”-GNFW pressure model. In doing so we try to disentangle the thermal pressure built-in correlation between pairs of physical parameters that lead to the SZ effect intensity—i.e. $(T_g, M_g), (f_g, M_T)$, etc.

6.1 Isothermal β -Model

Generally, there are two different parameterisations that one could use in the analysis of the cluster SZ effect and deriving its physical parameters. However, the assumption of isothermality provides another form of parameterisation where the gas temperature is assumed as an input free parameter along with the assumption of hydrostatic equilibrium (e.g. isothermal β -model or isothermal GNFW model).

In the following sections we discuss our three different param-

eterisations for the isothermal β -model within our Bayesian framework. It should be noted that in all of these parameterisations, we employ physically-based sampling parameters. Such parameters reveal the structure of degeneracies in the cluster parameter space more clearly than parameters that just describe the y -map such as angular core radius θ_c , shape β and central temperature decrement ΔT_0 . We also note that throughout our analysis we impose the additional constraint that the cluster has a non-zero r_{500} .

6.1.1 Parameterisation I

Our sampling parameters for this case are $\Theta_c \equiv (x_c, y_c, r_c, \beta, T_g, M_g(r_{200}), z)$, where x_c and y_c are cluster projected position on the sky, r_c and β are the parameters defining the density profile, T_g is the gas temperature, $M_g(r_{200})$ is the gas mass internal to radius r_{200} and z is the cluster redshift. It should be noted that AMI can typically measure the overdensity radii r_{500} and r_{200} for $z > 0.15$. However, we choose to work in terms of an overdensity radius of r_{200} since the constraints from AMI data on the cluster physical parameters are stronger at this radius and this radius is approximately the virial radius. We further assume that the priors on sampling parameters are separable (Feroz et al. 2009) such that

$$\pi(\Theta_c) = \pi(x_c) \pi(y_c) \pi(r_c) \pi(\beta) \pi(T_g) \pi(M_g(r_{200})) \pi(z). \quad (27)$$

This implies that parameterisation I ignores the known apriori correlation between the cluster total mass and gas temperature. We use Gaussian priors on cluster position parameters, centred on the pointing centre and with standard deviation of 1 arcmin. We adopt uniform priors on the cluster core radius, β and the gas temperature. As mentioned in Feroz et al. (2009), for SZ pointed observations, where we know the cluster redshift from optical studies and possibly the gas mass fraction from X-ray studies, we can assume a separable prior on the gas mass and redshift, namely, $\pi(M_g, z) \propto \pi(M = M_g/f_g, z) = \pi(M = M_g/f_g) \pi(z)$, (Feroz et al. 2009), where each factor has some simple functional form such that their product gives a reasonable approximation to a known mass function e.g. the Press–Schechter (Press & Schechter 1974) mass function. We will assume such a form in our analysis where $\pi(M_g)$ will be taken to be uniform in log in the range $(M_g)_{\min} = 10^{12} h^{-2} M_\odot$ to $(M_g)_{\max} = 5 \times 10^{14} h^{-2} M_\odot$ and the redshift is fixed to the cluster redshift. A summary of the priors and their ranges for this parameterisation is presented in Table 2.

Having established our physical sampling parameters, modelling the SZ signal is performed through the calculation of the y parameter which requires the knowledge of parameters describing the 3-D plasma density and its temperature, namely $r_c, \beta, n_e(0)$ and T_g . We sample from r_c, β and T_g but as shown below, deriving $n_e(0)$ requires employing the assumptions of hydrostatic equilibrium, isothermality and spherical geometry right from the beginning of the analysis.

Substituting the isothermal β -model into the equation of hydrostatic equilibrium equation (23), we can then relate the $M_T(r_{200})$ to our model parameters as well as to the temperature

$$M_T(r_{200}) = \frac{3\beta r_{200}^3}{r_c^2 + r_{200}^2} \frac{k_B T_g}{\mu G}, \quad (28)$$

where we have used $\varrho_g(r) = \mu_e n_e(r)$ with $\mu_e = 1.14 m_p$ (Jones et al. 1993; Mason & Myers 2000) defined as the mean gas mass per electron. By combining equations (25) and (28) at r_{200} , we first calculate the overdensity radius of r_{200} and since $M_g(r_{200})$ is also

Table 2. Summary of the priors on the sampling parameter set in parameterisation I. Note that $N(\mu, \sigma)$ represents a Gaussian probability distribution with mean μ and standard deviation of σ and $U(a, b)$ represents a uniform distribution between a and b .

Parameter	Prior
x_c, y_c	$N(0, 60)''$
r_c	$U(10, 1000) h^{-1} \text{kpc}$
β	$U(0.34, 2.5)$
$\log M_g(r_{200})$	$U(12, 14.5) h^{-2} M_\odot$
T_g	$U(0, 20) \text{keV}$

one of our sampling parameters we can recover the central electron number density by rearranging equation (24):

$$r_{200} = \sqrt{\frac{9\beta k_B T_g}{4\pi\mu_e G(200\varrho_{\text{crit}}(z))}} - r_c^2, \quad (29)$$

$$n_e(0) = \frac{M_g(r_{200})}{4\pi\mu_e \int_0^{r_{200}} \frac{r'^2 dr'}{\left(1 + \frac{r'^2}{r_c^2}\right)^{3\beta/2}}}. \quad (30)$$

For cluster physical parameters we use the value of the overdensity radius of r_{200} (equation 29) to calculate the cluster total mass internal to r_{200} assuming spherical geometry, (equation 25). The gas mass fraction at r_{200} is then simply $f_g(r_{200}) = M_g(r_{200})/M_T(r_{200})$. As the central electron number density and plasma temperature are assumed to be constants, we can in principle calculate cluster physical parameters in any overdensity radius other than r_{200} by assuming that the hydrostatic equilibrium holds everywhere in the cluster. In this paper we study the cluster properties at two overdensity radii r_{200} and r_{500} . Extracting cluster physical parameters at r_{500} in particular enables us to compare our results with the results obtained from X-ray analysis of the clusters of galaxies. r_{500} is calculated by equating equations (23) and (25) and setting $X = 500$. $M_g(r_{500})$ and $M_T(r_{500})$ are then derived using equations (24) and (25) respectively.

6.1.2 Parameterisations II and III

Parameterisation I does not take into account the correlation between the cluster total mass and its mean gas temperature. However, as mentioned earlier, observations of galaxy clusters and theoretical studies have both shown that there is a strong correlation between these two cluster parameters. We have already used this parameterisation in the analyses of 7 clusters out to the virial radius (AMI Consortium: Zwart et al. 2010). We found that using this parameterisation along side the assumption of isothermality led to strong biases in the estimation of cluster parameters. This implies that, in the absence of a measured temperature profile, we should eliminate gas temperature from the list of our sampling parameters and instead sample from either $M_T(r_{200})$ or $M_g(r_{200})$, and $f_g(r_{200})$. We choose total mass as a sampling parameter since this is consistent with our cluster detection algorithm and analysis (AMI Consortium: Shimwell et al. 2010). This form of parameterisation then allows us to calculate gas temperature either by using isothermal hydrostatic equilibrium (parameterisation II), or virial relation, (parameterisation III).

Our sampling parameters for these two parameterisations are $\Theta_c \equiv (x_c, y_c, r_c, \beta, M_T(r_{200}), f_g(r_{200}), z)$ which are assumed to be in-

Table 3. Summary of the priors on the sampling parameter set in parameterisations II and III.

Parameter	Prior
x_c, y_c	$N(0, 60)''$
r_c	$U(10, 1000) h^{-1} \text{kpc}$
β	$U(0.34, 2.5)$
$\log M_T(r_{200})$	$U(14, 15.5) h^{-1} M_\odot$
$f_g(r_{200})$	$N(0.084, 0.016) h^{-1}$

dependent for the same reasons described in previous section such that

$$\pi(\Theta) = \pi(x_c) \pi(y_c) \pi(r_c) \pi(\beta) \pi(M_T(r_{200})) \pi(f_g(r_{200})) \pi(z). \quad (31)$$

The priors on x_c, y_c, r_c, β and z are the same as for parameterisation I. The prior on $M_T(r_{200})$ is taken to be uniform in $\log M$ in the range $M_{\min} = 10^{14} h^{-1} M_\odot$ to $M_{\max} = 5 \times 10^{15} h^{-1} M_\odot$ and the prior of $f_g(r_{200})$ is set to be a Gaussian centred at the WMAP7 best fit value: $f_g = 0.12$ with a width of 0.016 (Komatsu et al. 2011; Larson et al. 2011 and AMI Consortium: Rodríguez-González et al. 2011). A summary of the priors and their ranges for these two parameterisations are presented in Table 3. We calculate $M_g(r_{200})$ from the definition of gas mass fraction and r_{200} is determined assuming spherical geometry, equation (25). Central electron number density is then calculated using equation (30).

For parameterisation II, the gas temperature at r_{200} is estimated assuming hydrostatic equilibrium using equation (28) and is assumed to be constant throughout the cluster

$$\begin{aligned} k_B T_g(r_{200}) &= \frac{\mu G M_T(r_{200})(r_{200}^2 + r_c^2)}{3\beta r_{200}^3} \\ &= \frac{(4\pi\mu G)(200Q_{\text{crit}}(z))(r_{200}^2 + r_c^2)}{9\beta}, \end{aligned} \quad (32)$$

where the last form is derived by substituting for $M_T(r_{200})$ using equation (25). We refer to relation (32) as the HSE mass-temperature relation. Similar to parameterisation I, once temperature and central electron number density are determined, we can calculate cluster physical properties at the overdensity radius of r_{500} using equations (23), (24) and (25) and setting $X = 500$.

For parameterisation III, we calculate the mean gas temperature within a virial radius of r_{200} using the mass-temperature relation described in equation (26), which is then assumed to be constant throughout the cluster

$$k_B T_g(r_{200}) = 8.2 \left(\frac{M_T(r_{200})}{10^{15} h^{-1} M_\odot} \right)^{2/3} \left(\frac{H(z)}{H_0} \right)^{2/3} \text{ keV}. \quad (33)$$

We refer to this relation as the virial mass-temperature relation. This also implies that virialisation occurs at r_{200} . In our analysis, we use this relation to determine the mean gas temperature and once this is determined we repeat the same procedure carried out for parameterisations I and II to obtain cluster physical properties at the overdensity radius r_{500} .

6.2 Entropy-GNFW Pressure Model

As it was mentioned in Section 5.2 the choice of the GNFW pressure profile to model the SZ signal is reasonable as the SZ surface brightness is proportional the line of sight integral of the electron pressure. However, in order to link the gravitational potential shape

to the baryonic physical properties of the ICM, one has to make assumptions on the radial profile of another thermodynamical quantity. Among the thermodynamical quantities of the ICM, entropy has proved to be an important gas property within the cluster. Entropy is conserved during the adiabatic collapse of the gas into the cluster gravitational potential well, however, it will be affected by any non-gravitational processes such as radiative cooling, star formation, energy feed back from supernovae explosions and Active Galactic Nuclei (AGN) activities. It therefore keeps a record of the thermodynamic history of the ICM (Voit 2000; 2003, 2005; Ponmann et al. 1999; Pratt & Arnaud 2002; Allison et al. 2011).

Moreover, for a gravitationally collapsed gas in hydrostatic equilibrium, entropy profile is expected to have an approximate power law distribution ($\approx r^{-1.1}$) (Lloyd-Davies et al. 2000; Voit 2005; Nagai et al. 2007; Pratt 2010). However, there is a large deviation from self-similarity in the entropy radial profile in the inner region of the cluster ($r < 0.1 r_{200}$) due to the impact of all of the non-gravitational mechanisms described above on the thermodynamics of the ICM (Finoguenov et al. 2002; Ponman et al. 1999, 2003; Lloyd-Davies et al. 2000; Pratt 2010). In the inner region, the results of the non-radiative simulations and simulations that take into account AGN activities plus preheating models predict a flat core in the entropy distribution due to entropy mixing (Wadsley et al. 2008; Mitchell et al. 2009). The observed entropy profiles using X-ray telescopes also flatten in the inner regions in general while having similar external slopes (Pratt et al. 2006). In the outskirts of the cluster (out to virial radius and beyond), on the other hand, the results of the latest numerical simulations (Nagai 2011; Nagai et al. 2011) and observational studies of the clusters using *Suzaku* and XMM-Newton satellites at large radii including A1795 (Bautz et al. 2009), PKS 0745-191 (George et al. 2009), A2204 (Reiprich et al. 2009), A1413 (Hoshino et al. 2010), A1689 (Kawaharada et al. 2010), Virgo cluster (Urban et al. 2011) and Perseus cluster (Simionescu et al. 2011) also show that behaviour of ICM entropy deviates from the prediction of a spherically systematic shock heated gas model (Tozzi & Norman 2001). According to these studies major sources of this deviation may be due to incomplete virialisation, departure from hydrostatic equilibrium, gas motion and gas clumping.

In this context and to derive the cluster physical parameters we decided to adopt the entropy profile presented in Allison et al. (2011) which is a β - model like profile:

$$K_e(r) = K_{ei} \left(1 + \frac{r^2}{r_c^2} \right)^\alpha, \quad (34)$$

where $K_e(r)$ is the plasma entropy at radius r , K_{ei} is the normalisation coefficient of the entropy profile, r_c and α are the parameters defining the shape of the profile at different radii. Assuming an entropy profile with above form guarantees the flat shape in the inner region and a power law distribution at the larger radii (up to r_{500}) where $K_e(r) \propto r^{2\alpha}$ with $\alpha \sim 0.55$. We note that in order to take into account the behaviour of entropy at the clusters outskirts we need to modify the assumed entropy profile with additional parameter and/or component. However, as the studies of this kind in understanding the physics of the cluster outskirts and accurate measurements of the ICM profiles in the cluster outer regions are still ongoing, we do not study a modified form of our assumed entropy profile here. We of course aim to consider a more general form in our future analyses.

As for using the GNFW profile, one has indeed to make an assumption on either the density, temperature or the entropy profile shape in order to link the gravitational potential shape to the baryonic physical properties of the ICM. In this paper, we decided

Table 4. Summary of the priors on the sampling parameter set in the entropy-GNFW pressure model.

Parameter	Prior
x_c, y_c	$N(0, 60)''$
r_c	$U(10, 1000) h^{-1} \text{kpc}$
α	$U(0.0, 1.0)$
$\log M_T(r_{200})$	$U(14, 15.5) h^{-1} M_\odot$
$f_g(r_{200})$	$N(0.084, 0.016) h^{-1}$
r_p	$U(0.001, 3) h^{-1} \text{Mpc}$

to work with an assumption of entropy profile for all the reasons given above. The combination of the GNFW pressure and the “ α -model” entropy profiles can then fully describe the large-scale properties of clusters as they determine the form of the dark matter potential well in addition to the structure of the ICM.

To relate the entropy to the other thermodynamical quantities inside the ICM we use the definition of the entropy given in the astronomy literature. For an adiabatic monatomic gas,

$$K_e = k_B T n_e^{-2/3} \quad (35)$$

$$P_e = K_e n_e^{5/3}, \quad (36)$$

which is related to the true thermodynamic entropy per gas particle via $S = \frac{3}{2} k_B \ln(K_e) + S_0$ where S_0 is a constant (Voit 2005).

Using equations (20),(34),(35) and (36) we can derive the 3-D radial profiles of the electron number density and the temperature,

$$n_{ei}(r) = n_{ei} \left(\frac{r}{r_p} \right)^{\left(\frac{-2}{5}\right)c} \left[1 + \left(\frac{r}{r_p} \right)^a \right]^{-\frac{3}{5} \left(\frac{b-c}{a} \right)} \left[1 + \left(\frac{r}{r_c} \right)^2 \right]^{-\frac{3}{5}\alpha} \quad (37)$$

$$k_B T_{ei}(r) = k_B T_{ei} \left(\frac{r}{r_p} \right)^{\left(\frac{-2}{5}\right)c} \left[1 + \left(\frac{r}{r_p} \right)^a \right]^{-\frac{2}{5} \left(\frac{b-c}{a} \right)} \left[1 + \left(\frac{r}{r_c} \right)^2 \right]^{-\frac{3}{5}\alpha} \quad (38)$$

where

$$n_{ei} = \left(\frac{P_{ei}}{K_{ei}} \right)^{\frac{3}{5}} \quad (39)$$

and

$$k_B T_{ei} = P_{ei}^{2/5} K_{ei}^{3/5} \quad (40)$$

are the normalisation coefficients for the electron number density and the temperature profiles respectively. We note that the above derived electron number density has components that take into account both the fit for the inner slope of the cuspy cluster density profiles and the steepening at larger radii ($r \geq r_{500}$) (Pratt & Arnaud 2002, Vikhlinin et al. 2006).

As using this model to analyse the cluster SZ signal removes the assumption of isothermality, parameterisation I which assumes a single core temperature as a free input parameter can not be used in the analysis using entropy-GNFW model or any non- isothermal model. We therefore study the cluster SZ signal and its physical properties using parameterisations II and III.

Our sampling parameters for this model are $\Theta_c \equiv (x_c, y_c, r_c, \alpha, M_T(r_{200}), f_g(r_{200}), z)$. A summary of the priors and their ranges for the “entropy”-GNFW pressure model is presented in Table 4.

$$\pi(\Theta_c) = \pi(x_c) \pi(y_c) \pi(r_c) \pi(\alpha) \pi(M_T(r_{200})) \pi(f_g(r_{200})) \pi(z). \quad (41)$$

Sampling from $M_T(r_{200})$ in both parameterisations leads to the estimation of r_{200} assuming spherical geometry for the cluster, equation (25). Sampling from $M_T(r_{200})$ and $f_g(r_{200})$ also allows us to calculate $M_g(r_{200})$. n_{ei} is then

$$n_{ei} = \frac{M_g(r_{200})}{4\pi\mu_e \int_0^{r_{200}} r'^2 \left(\frac{r'}{r_p} \right)^{\left(\frac{-2}{5}\right)c} \left[1 + \left(\frac{r'}{r_p} \right)^a \right]^{-\frac{3}{5} \left(\frac{b-c}{a} \right)} \left[1 + \left(\frac{r'}{r_c} \right)^2 \right]^{-\frac{3}{5}\alpha} dr'} \quad (42)$$

In parameterisation II we substitute the electron number density and GNFW pressure profiles in the assumption of hydrostatic equilibrium ($\frac{1}{\rho_{\text{gas}}} \frac{dP_{\text{gas}}}{dr} = -\frac{GM_{\text{tot}}}{r^2}$) at r_{200} and derive P_{ei} . The normalisation coefficients for the temperature and entropy profiles, $k_B T_{ei}$ and K_{ei} , are then calculated by solving the equations (39) and (40) simultaneously.

In parameterisation III we calculate $k_B T_{ei}(r_{200})$ using virial M-T relation, equation(33). $k_B T_{ei}$ is then calculated by substituting the values derived for r_{200} and $k_B T_{ei}(r_{200})$ in temperature profile given in equation (38). Similarly, the normalisation coefficients for the pressure and entropy profiles, P_{ei} and K_{ei} , are then calculated by solving the equations (39) and (40) simultaneously.

In order to estimate the cluster physical parameters at r_{500} we use the definition of gas concentration parameter c_{500} to estimate r_{500} ,

$$c_{500} = \frac{r_{500}}{r_p}. \quad (43)$$

We fix c_{500} to the value given in Arnaud et al. (2010) ($c_{500} = 1.156$). With knowledge of r_{500} and all the four normalisation coefficients ($P_{ei}, K_{ei}, k_B T_{ei}, n_{ei}$) we can calculate $M_T(r_{500}), M_g(r_{500}), f_g(r_{500})$ and $k_B T_{500}$.

7 SIMULATED AMI SA DATA

In generating simulated SZ skies and observing them with a model AMI SA, we have used the methods outlined in Hobson & Masingier (2002) and Grainge et al. (2002).

Generating a simulated cluster SZ signal using the isothermal β -model requires the input parameters of $z, T_g, n_e(0), r_c,$ and β ; this set of parameters fully describes the Comptonisation y parameter. However, in order to verify the results of our analysis and to see if our methodology is capable of recovering the true values associated with the simulated cluster, it is instructive to estimate the cluster physical parameters using the three parameterisation discussed. We note that any parameterised model within the hierarchical structure formation of the universe for the ICM, including the isothermal β -model, introduces constraints and biases in the inferred cluster parameters. Moreover, we now show that it is possible to get different cluster physical parameters with the same set of input model parameters derived using the two different mass-temperature relations described in Section 6.1.2.

For example, if we consider parameterisation II we can use the HSE mass-temperature relation to calculate r_{200} given in equation (29). $M_g(r_{200})$ and $M_T(r_{200})$ are then calculated applying spherical geometry assumptions described in equations (24) and (25) respectively. We can also determine $f_g(r_{200})$.

However, if we consider parameterisation III we first calculate $M_T(r_{200})$ using the virial mass-temperature relation given in equation (33). r_{200} and $M_g(r_{200})$ are then estimated assuming spherical geometry for the cluster, (equations 25 and 24). A numerical example that leads to different results in cluster parameters is given in Table 5. To address this issue, we studied how $f_g(r_{200})$ varies as a function of r_c and β while $n_e(0), T_g$ and z are fixed for both the HSE and virial M-T relations. Clearly, to obtain consistent results from both parameterisations one should select the values of r_c and β for which the corresponding gas mass fraction ratio is one.

Table 5. An example of input cluster parameters for the isothermal β -model that lead to inconsistent results using different parameterisations assuming $h = 0.7$.

Input parameter	Assumed value	Derived parameter	Parameterisation I,II	Parameterisation III
x_c	0	r_{200}	1.56 Mpc	1.71 Mpc
y_c	0			
r_c	200 kpc	$M_T(r_{200})$	$5.83 \times 10^{14} M_\odot$	$7.67 \times 10^{14} M_\odot$
β	0.95			
T_g	5 keV	$M_g(r_{200})$	$5.91 \times 10^{13} M_\odot$	$6.28 \times 10^{13} M_\odot$
$n_e(0)$	10^4 m^{-3}			
z	0.3	$f_g(r_{200})$	0.102	0.082

Table 6. Cluster parameters for the isothermal β -model assuming $h = 0.7$.

Input Parameter	Assumed value	Derived Parameter	Parameterisation I,II,III
x_c	0	r_{200}	1.56 Mpc
y_c	0	$M_T(r_{200})$	$5.83 \times 10^{14} M_\odot$
r_c	155 kpc	$M_g(r_{200})$	$6.36 \times 10^{13} M_\odot$
β	0.79	$f_g(r_{200})$	0.109
T_g	5 keV	r_{500}	0.98 Mpc
$n_e(0)$	10^4 m^{-3}	$M_T(r_{500})$	$3.64 \times 10^{14} M_\odot$
z	0.3	$M_g(r_{500})$	$4.13 \times 10^{13} M_\odot$
		$f_g(r_{500})$	0.11

It should be noted that the same study may be carried out by investigating the variation of the ratio of gas mass fractions with either $n_e(0)$ or T_g while keeping r_c and β constant. However we find that the ratio is not sensitive to variation of these two parameters.

Given the above, we decided to generate a simulated cluster with input parameters given in Table 6, which leads to consistent physical parameters for the cluster, at both r_{200} and r_{500} in both parameterisations. We assume that our cluster target is at declination $\delta = +40^\circ$ observed for hour angles between -4 and $+4$ with 2-s sampling for four days and 8 hours per day. We calculate the Comptonisation y parameter on a grid of 512×512 pixels with pixel size of $30''$. A realisation of the primary CMB is calculated using a power spectrum of primary anisotropies which was generated for $l < 8000$ using CAMB (Lewis, Challinor & Lasenby 2000), with a Λ CDM cosmology: $\Omega_M = 0.3$, $\Omega_\Lambda = 0.7$, $\sigma_8 = 0.8$, $H_0 = 70 \text{ km s}^{-1} \text{ Mpc}^{-1}$, $w_0 = -1$ and $w_a = 0$. The CMB realisation is then co-added to the cluster in brightness temperature. It should be noted that in our simulation we did not include extragalactic radio sources, or diffuse foreground emission from the galaxy as we have already addressed the effects of the former in Feroz et al. 2009 and the foreground galactic emission is unlikely to be a major contaminant since our interferometric observations resolve out such large scale emission. The map is scaled by the primary beam appropriate to the measured value in the frequency channel and transformed into the Fourier plane. The resulting distribution is sampled at the required visibility points and thermal noise of 0.54 Jy per channel per baseline in one second which is appropriate to the measured sensitivity of the SA is added. Fig. 1 shows a map of the SZ temperature decrement of the first simulated cluster generated using the isothermal β -model.

To generate the second simulated cluster we use the GFWF pressure profile to calculate the Comptonisation y parameter. The input parameters for this model, (P_{ei} , r_p), were selected to represent

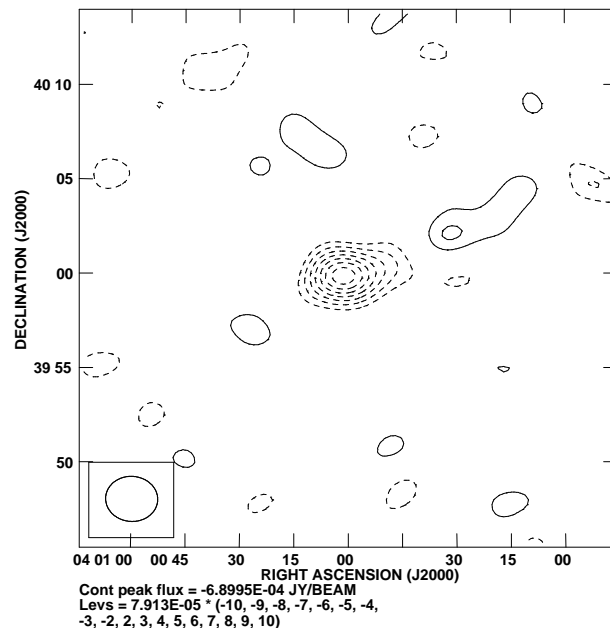


Figure 1. Map of the simulated AMI SZ temperature decrement generated with the isothermal- β model and parameters given in Table 6. Contours at $\dots -3, -2, 2, 3, \dots$ times noise ($\sigma = 79 \mu\text{Jy beam}^{-1}$), negative contours are dashed. The coordinates are J2000.0.

Table 7. Cluster parameters for the entropy-GFWF model assuming $h = 0.7$.

Input parameter	Assumed value	Derived parameter	"Entropy"-GFWF model
x_c	0	r_{200}	1.56 Mpc
y_c	0	$M_T(r_{200})$	$5.83 \times 10^{14} M_\odot$
r_p	0.85 Mpc	$M_g(r_{200})$	$6.36 \times 10^{13} M_\odot$
P_{ei}	$37647.51 \text{ keV m}^{-3}$	$f_g(r_{200})$	0.109
z	0.3	r_{500}	0.98 Mpc
r_c	155 kpc	$M_T(r_{500})$	$3.64 \times 10^{14} M_\odot$
α	0.55	$M_g(r_{500})$	$4.08 \times 10^{13} M_\odot$
T_{200}	5 keV	$f_g(r_{500})$	0.11
		T_{500}	6.95 keV

a cluster with the same physical parameters at r_{200} and the same noise level as the first cluster. Although the parameters r_c , α , z , and $T_c(r_{200})$ do not contribute to the calculation of Comptonisation y parameter directly, their values were used to derive the parameters describing the GFWF pressure profile by following the steps described in section 6.2 to ensure that they represent the cluster with required physical parameters at r_{200} . The cluster physical parameters at different radii will be different from the first cluster due to the different models describing the ICM and relaxing the assumption of isothermality in the second cluster. A summary of the cluster parameters is presented in Table 7. Fig. 2 shows a map of the SZ temperature decrement of the second simulated cluster, generated using the GFWF model.

8 ANALYSIS AND RESULTS

In this section we present the results of our analysis for all three parameterisations within the context of the isothermal β -model and

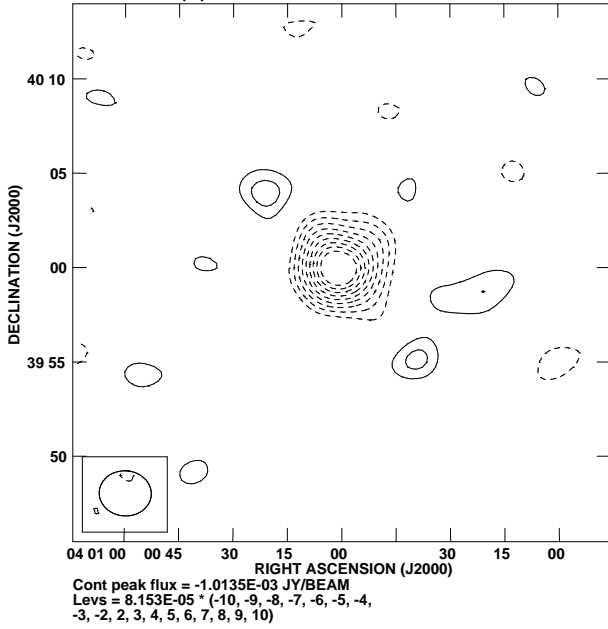


Figure 2. Map of the simulated AMI SZ temperature decrement generated with GFW model and parameters given in Table 7. Contours at ... -3, -2, 2, 3... times noise ($\sigma = 81.5 \mu\text{Jy beam}^{-1}$), negative contours are dashed. The coordinates are J2000.0.

the entropy-GFW pressure model. In each case we first study our methodology in the absence of data. This can be carried out by setting the likelihood to a constant value and hence the algorithm explores the prior space. This analysis is crucial for understanding the underlying biases and constraints imposed by the priors and the model assumptions. Along with the analysis done using the simulated AMI data, this approach reveals the constraints that measurements of the SZ signal place on the cluster physical parameters and the robustness of the assumptions made. It should be noted that in all the plots of probability distributions, we explicitly include the dimensionless Hubble parameter $h = H_0/(100 \text{ km s}^{-1} \text{ Mpc}^{-1})$ with h set to 1.0.

8.1 Analysis using isothermal β -model-Parameterisation I

Figs. 3 and 4 represent the results of a priors-only analysis showing the sampling and derived parameters respectively. 1-D marginalised posterior distributions of sampling parameters in Fig. 3 show that we were able to recover the assumed prior probability distributions for cluster position and the gas mass. However, this parameterisation clearly prefers higher temperature and β and the probability distribution for r_c falls as we go towards higher r_c . This feature in particular creates a void region in the 2-D marginalised probability distributions of $\beta - r_c$ and $T_g - r_c$ at higher r_c which implies that low mass clusters are unlikely to have high r_c and low β . This effect is a direct result of imposing the constraint that $r_{500} > 0$. Moreover, as may be seen from Fig. 4, this choice of priors drives the posterior probability distributions of both the gas mass and the gas mass fraction towards low values.

Figs. 5 and 6 show the results of the analysis of the simulated SZ cluster data. The vertical lines show the true values of the parameters. Table 8 also summarises the mean, the dispersion and the maximum likelihood of each parameter.

In Fig. 5, we notice the strong degeneracy between r_c and β

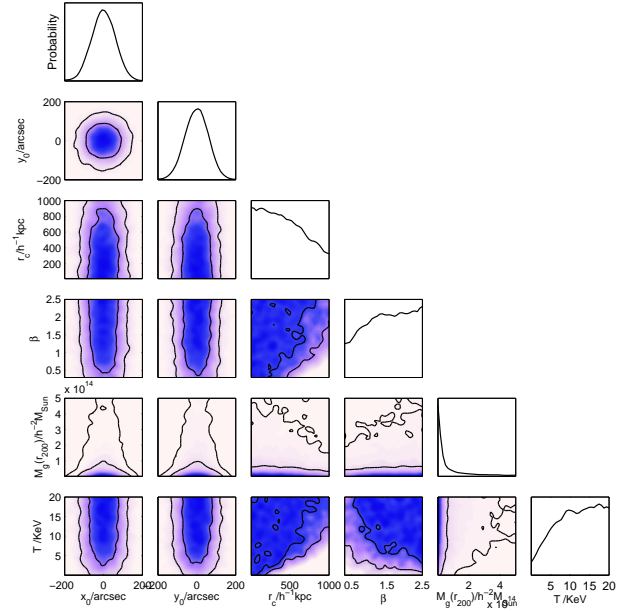


Figure 3. Marginal distributions for the sampling parameters with no data for isothermal β -model –parameterisation I.

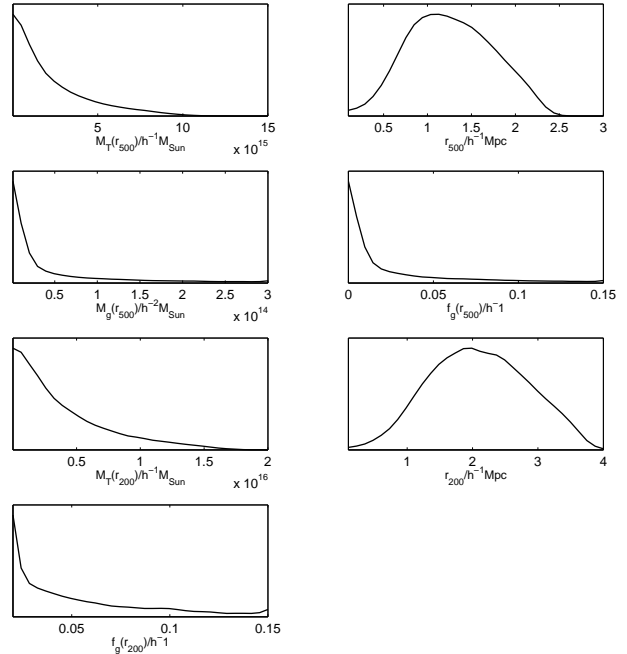


Figure 4. Marginal distributions for the derived cluster physical parameters with no data for isothermal β -model –parameterisation I.

(Grego et al. 2001). However, it is apparent that neither β nor T_g is well-constrained using this parameterisation. Also, higher values than the true input parameters are preferred for both parameters. This effect leads to two results: firstly it yields a higher estimate for r_{200} and so equation (28) overestimates the total mass; secondly, since for this parameterisation there is a negative degeneracy between gas mass and temperature, the high temperature therefore leads the marginalised posterior distribution for gas mass peaking towards the lower end of the distribution although the recovered mean value of $M_g(r_{200})$ is within 1σ from its corresponding input value for the simulated cluster. As a result of these two effects, the

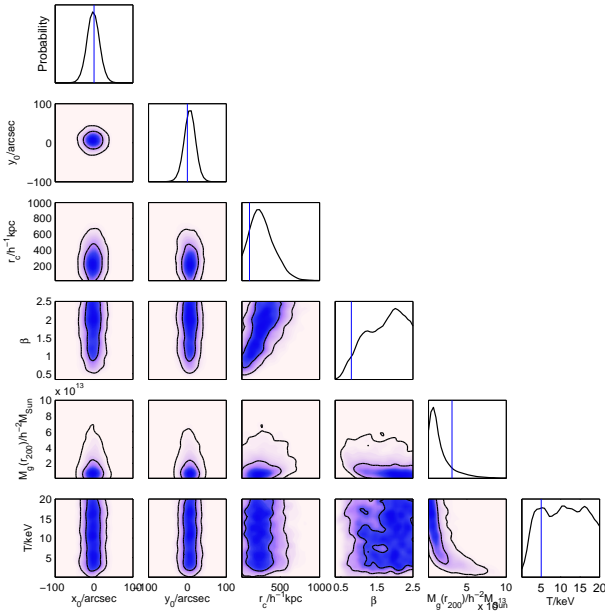


Figure 5. Marginal distributions of the sampling parameters for simulated data for isothermal β -model –parameterisation I.

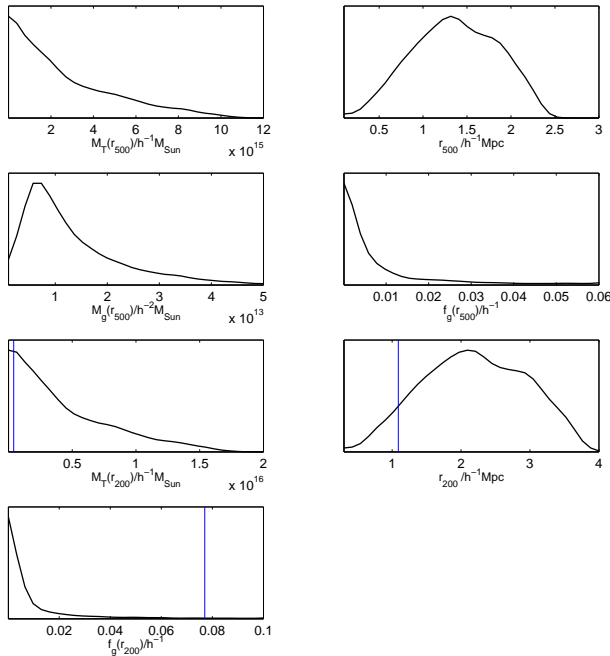


Figure 6. Marginal distributions of the derived cluster physical parameters with simulated data for isothermal β -model –parameterisation I.

gas mass fraction is driven even further to the lower end of the allowed range. There is also a degeneracy between the two free parameters of β and T_g ; this degeneracy again originates from dependency of r_{200} on both parameters as given in equation (29).

8.2 Analysis using isothermal β -model-Parameterisation II

Figs. 7 and 8 show the results from prior-only analysis for parameterisation II. We recover the assumed prior probability distributions for cluster position, β , total mass and gas mass fraction. There is a similar trend in the 1-D posterior probability distribution of r_c to

Table 8. Simulated cluster parameters (mean, standard deviation and Maximum likelihood) estimated using isothermal β -model–parameterisation I assuming $h = 0.7$.

Parameter	$\mu \pm \sigma$	$\hat{\mu}$
x_c	$-2.1 \pm 15.3''$	$-0.6''$
y_c	$6.3 \pm 13.9''$	$5.5''$
r_c	391.26 ± 214.98 kpc	138.77 kpc
β	1.7 ± 0.5	0.98
$M_g(r_{200})$	$(3.41 \pm 3.16) \times 10^{13} M_\odot$	$2.86 \times 10^{13} M_\odot$
T_g	10.61 ± 5.28 keV	10.15 keV
$M_T(r_{500})$	$(3.91 \pm 3.41) \times 10^{15} M_\odot$	$1.49 \times 10^{15} M_\odot$
r_{500}	1.96 ± 0.69 Mpc	1.57 Mpc
$M_g(r_{500})$	$(2.71 \pm 1.42) \times 10^{13} M_\odot$	$2.31 \times 10^{13} M_\odot$
$f_g(r_{500})$	0.15 ± 2.7	0.014
$M_T(r_{200})$	$(6.43 \pm 5.43) \times 10^{15} M_\odot$	$2.37 \times 10^{15} M_\odot$
r_{200}	3.14 ± 1.0 Mpc	2.49 Mpc
$f_g(r_{200})$	(0.14 ± 3.4)	0.012

Table 9. Simulated cluster parameters (mean, standard deviation and Maximum likelihood) estimated using isothermal β -model–parameterisation II assuming $h = 0.7$.

Parameter	$\mu \pm \sigma$	$\hat{\mu}$
x_c	$-2.6 \pm 15.7''$	$5.5''$
y_c	$6.4 \pm 14.5''$	$5.6''$
r_c	410.37 ± 237.24 kpc	135.43 kpc
β	1.7 ± 0.5	0.8
$M_T(r_{200})$	$(6.8 \pm 2.1) \times 10^{14} M_\odot$	$5.0 \times 10^{14} M_\odot$
$f_g(r_{200})$	0.12 ± 0.03	0.11
$M_T(r_{500})$	$(3.5 \pm 8.81) \times 10^{13} M_\odot$	$3.13 \times 10^{14} M_\odot$
r_{500}	0.96 ± 0.08 Mpc	0.93 Mpc
$M_g(r_{500})$	$(6.2 \pm 1.6) \times 10^{13} M_\odot$	$3.9 \times 10^{13} M_\odot$
$f_g(r_{500})$	0.18 ± 0.05	0.12
r_{200}	1.59 ± 1.57 Mpc	1.47 Mpc
$M_g(r_{200})$	$(7.76 \pm 2.08) \times 10^{13} M_\odot$	$5.35 \times 10^{13} M_\odot$
T_g	3.0 ± 1.2 keV	4.3 keV

that mentioned in the parameterisation I, which leads to a void region in the 2-D marginalised posterior distribution of $M_T(r_{200}) - r_c$ for the same reason as discussed for the parameterisation I. However, parameterisation II prefers a lower temperature which arises from the fact that HSE mass-temperature relation used in this parameterisation (equation 32) is inversely proportional to β .

Figs. 9 and 10 show the results of the analysis using simulated SZ cluster data, with vertical lines representing the true parameter values. Table 9 also summarises the mean, the dispersion and the maximum likelihood values of each cluster parameter estimated using parameterisation II. A tight degeneracy between r_c and β is noticeable in the corresponding 2-D marginalised probability distribution. β on the other hand is not well constrained and moves towards higher values which results in the probability distribution of temperature being driven to lower values again because of the $1/\beta$ relationship in equation (32). However, this parameterisation along with the simulated SZ data reliably constrains $M_T(r_{200})$, $M_g(r_{200})$ and $f_g(r_{200})$. Comparing the 1-D marginalised posterior distributions of gas mass fractions at two overdensity radii r_{500} and r_{200} also reveals that we cannot constrain the radial behaviour of the gas mass fraction using this parameterisation, as $f_g(r_{500})$ exhibits too wide a probability distribution. For $f_g(r_{200})$, we seem to have recovered the input prior distribution.

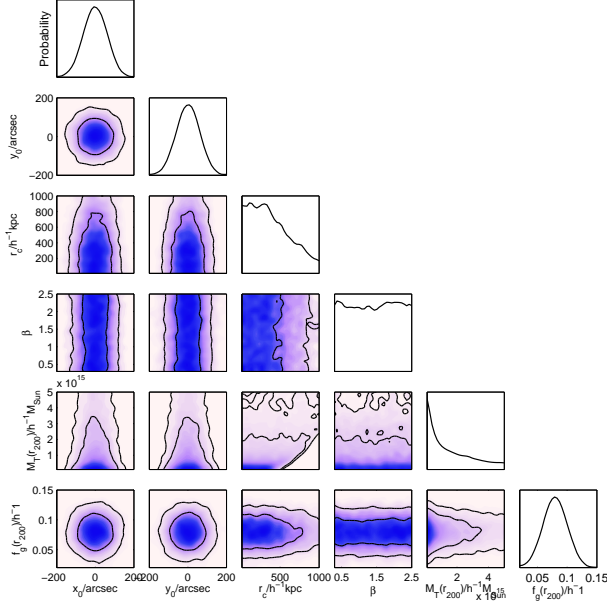


Figure 7. Marginal distributions of the sampling parameters with no data for isothermal β -model- parameterisation II.

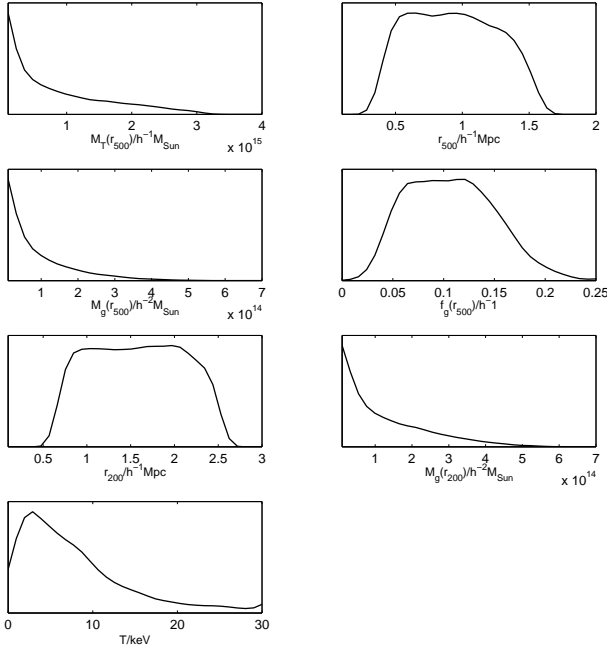


Figure 8. Marginal distributions of the derived cluster physical parameters with no data for isothermal β -model-parameterisation II.

8.3 Analysis using isothermal β -model-Parameterisation III

The results of the analysis with no data are plotted in Figs. 11 and 12. It is evident that, while the assumed prior probability distributions for the cluster position, total mass and gas mass fraction are recovered, the two sampling parameters r_c and β show the same behaviours as discussed for the other two parameterisations. We also see a trend towards lower values in the 1-D posterior probability distribution of temperature. However this behaviour is due to the direct relationship between the total mass and the temperature in this parameterisation and the specific prior distribution we have as-

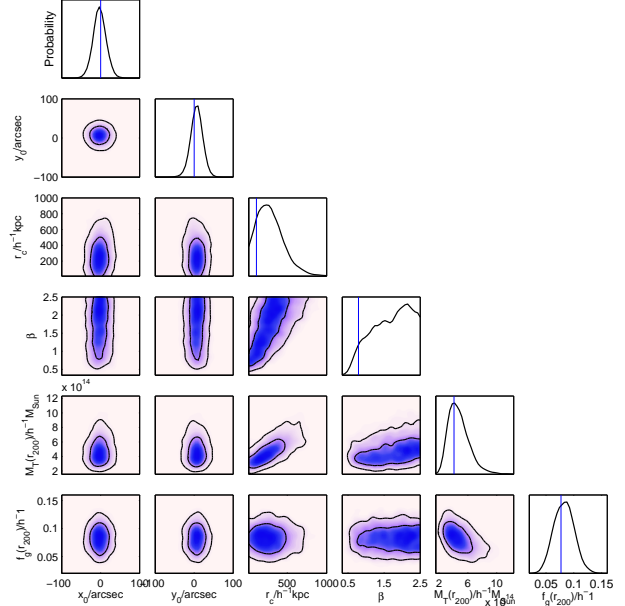


Figure 9. Marginal distributions of the sampling parameters with simulated data for isothermal β -model- parameterisation II.

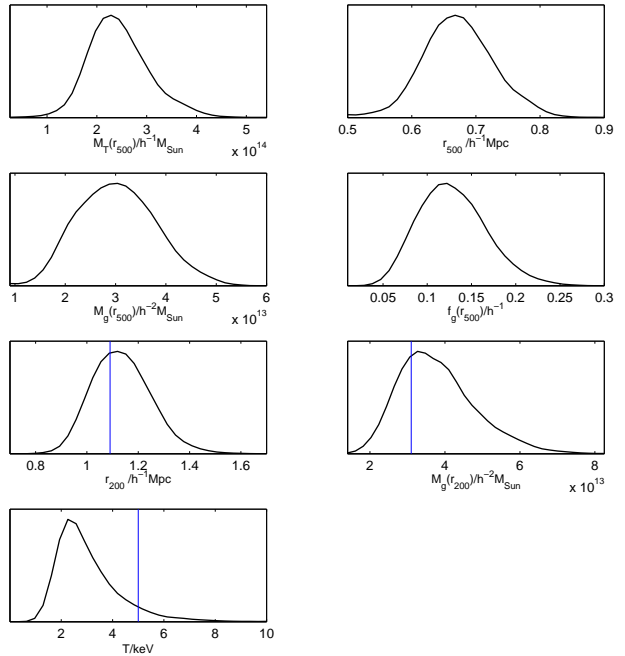


Figure 10. Marginal distributions of the derived cluster physical parameters with simulated data for isothermal β -model-parameterisation II.

sumed for the total mass which clearly has a higher probability at the lower masses.

Figs. 13 and 14 represent the marginalised posterior distributions from the analysis of simulated SZ cluster data for sampling and derived parameters respectively while in Table 10 we present the mean, the dispersion and the maximum likelihood of each cluster parameter estimated using parameterisation III. The strong degeneracy between r_c and β is quite apparent in this parameterisation, while β is poorly constrained and biased towards higher values. We note that, since the SZ analysis constrains cluster total mass internal to the radius r_{200} and we use the virial M-T relation (equa-

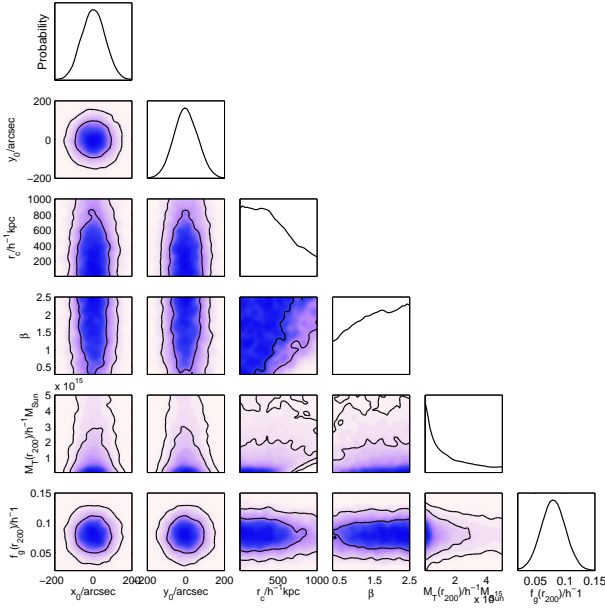


Figure 11. Marginal distributions of the sampling parameters with no data for isothermal β -model- parameterisation III.

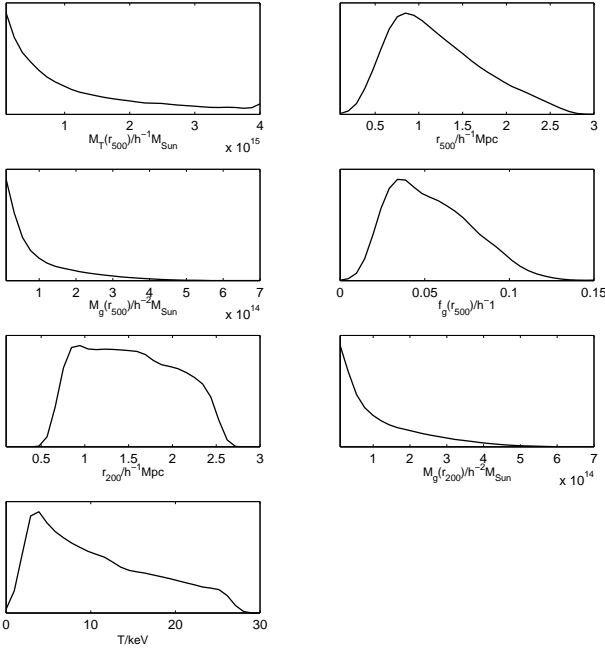


Figure 12. Marginal distributions of the derived cluster physical parameters with no data for isothermal β -model- parameterisation III.

tion (33)) to derive cluster average temperature within this radius, the result of temperature estimation is less biased and more reliable than the parameterisations I and II in recovering the temperature true value. We have used this parameterisation in our follow-up analysis of the real data where we studied a joint weak gravitational lensing and SZ analysis of six clusters (AMI Consortium: Hurley-Walker et al. 2011) and high and moderate X-ray luminosity sample of LoCuSS clusters (AMI Consortium: Rodríguez-González et al. 2011; AMI Consortium: Shimwell et al. 2011).

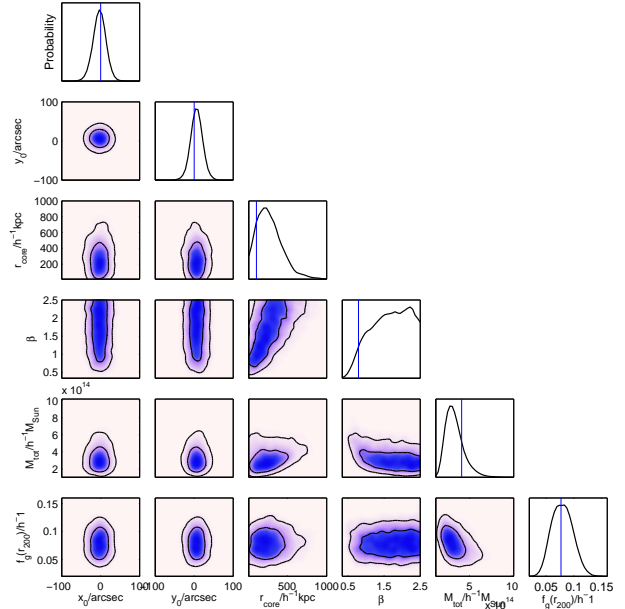


Figure 13. Marginal distributions of the sampling parameters with simulated data for isothermal β -model- parameterisation III.

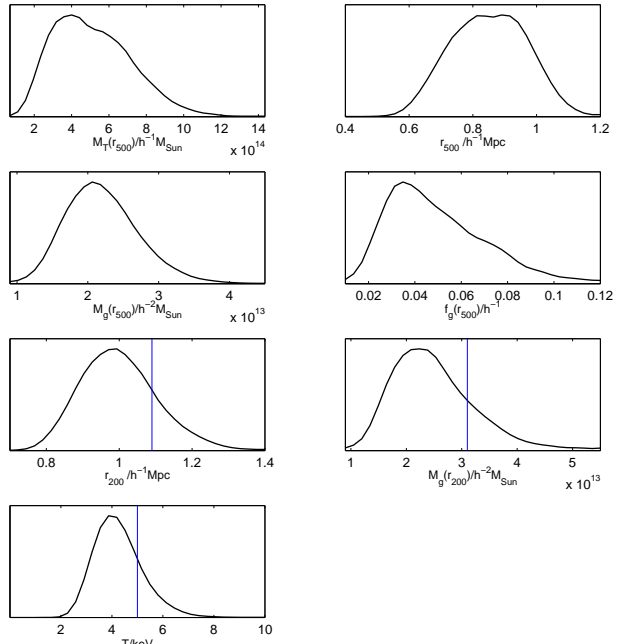


Figure 14. Marginal distributions of the derived cluster physical parameters with simulated data for isothermal β -model- parameterisation III.

8.4 Analysis using entropy-GNFW pressure model

Similar to the isothermal β -model we first studied our methodology for the "entropy"-GNFW pressure model with no data. The results are represented in Figs. 15 and 16. This analysis again helps us understand which parameters are constrained by SZ measurement as well as to check the algorithm in retrieving the prior probability distributions. From both 1-D and 2-D marginalised probability distributions it is clear that we are able to recover the input priors probability distributions and the probability distributions of the

Table 10. Simulated cluster parameters estimated (mean, standard deviation and Maximum likelihood) using isothermal β -model-parameterisation III assuming $h = 0.7$.

Parameter	$\mu \pm \sigma$	$\hat{\mu}$
x_c	$-3.0 \pm 15.6''$	$-5.0''$
y_c	$6.4 \pm 14.4''$	$5.7''$
r_c	395.11 ± 226.21 kpc	142.14 kpc
β	1.7 ± 0.5	1.1
$M_T(r_{200})$	$(4.68 \pm 1.56) \times 10^{14} M_\odot$	$4.46 \times 10^{14} M_\odot$
$f_g(r_{200})$	0.11 ± 0.03	0.1
$M_T(r_{500})$	$(7.35 \pm 3.0) \times 10^{14} M_\odot$	$4.58 \times 10^{14} M_\odot$
r_{500}	1.21 ± 0.17 Mpc	1.06 Mpc
$M_g(r_{500})$	$(4.50 \pm 1.04) \times 10^{13} M_\odot$	$4.00 \times 10^{13} M_\odot$
$f_g(r_{500})$	0.07 ± 0.03	0.09
r_{200}	1.43 ± 1.50 Mpc	1.42 Mpc
$M_g(r_{200})$	$(5.14 \pm 1.6) \times 10^{13} M_\odot$	$4.49 \times 10^{13} M_\odot$
T_g	4.3 ± 0.9 keV	4.2 keV

derived parameters are according to their corresponding functional dependencies on the sampling parameters.

Figs. 17, 18 and Table 11 show the results of our analysis for "entropy"-GNFW pressure profile using parameterisation II while Figs. 19, 20 and Table 12 show the results of the same analysis using parameterisation III. We note that in both analyses r_c and α the parameters that define the shape of the entropy profile are not constrained while the scaling radius, r_p , which defines the GNFW pressure profile is completely constrained. As a result we notice similar constraints in the estimation of r_{500} in both parameterisations since we assume a fixed c_{500} . We also note the degeneracies between $M_T(r_{200})$ - r_c and $M_T(r_{200})$ - α which are because of the dependency of P_{ei} on these two free parameters. On the other hand the $M_T(r_{200})$ - r_p degeneracy seen in Figs. 17 and 19 is due to the intrinsic degeneracy that exists between the cluster size and the volume integrated Comptonisation parameter (Y_{SZ} - r_p degeneracy) in the SZ measurements (Planck Collaboration 2011d). Moreover, comparing $T_g(r_{500})$ and $T_g(r_{200})$ (Table 11 and 12) confirms a radial decline in the ICM temperature distribution as expected.

Overall, both parameterisations could constrain the cluster physical parameters, however, analysis using parameterisation III leads to a tighter constrain on both $T_g(r_{500})$ and $T_g(r_{200})$. The results of Parameterisation III once more show that this parameterisation can reliably be used in the analysis of clusters of galaxies as it is less model dependent and produces unbiased results in particular when the assumption of hydrostatic equilibrium breaks, in young or disturbed clusters (parameterisation II).

9 DISCUSSION AND CONCLUSIONS

We have studied two parameterised models, the traditional isothermal β -model and the "entropy"-GNFW pressure model, to analyse the SZ effect from galaxy clusters and extract their physical parameters using AMI SA simulated data. In our analysis we have described the current assumptions made on the dynamical state of the ICM including spherical geometry, hydrostatic equilibrium and the virial mass-temperature relation. In particular we have shown how different parameterisations which relate the thermodynamical quantities describing the ICM to the cluster global properties via these assumptions lead to biases on the cluster physical parameters within a particular model.

In this context, we first generated a simulated cluster using

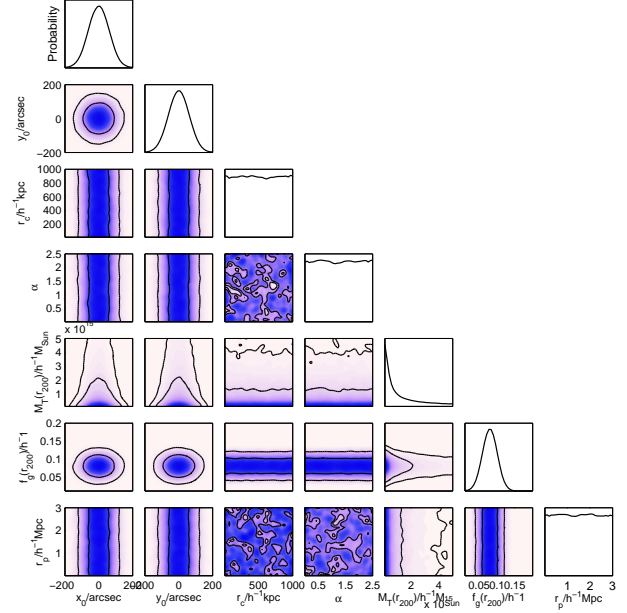


Figure 15. Marginal distributions of the sampling parameters with no data for "entropy"- GNFW pressure model.

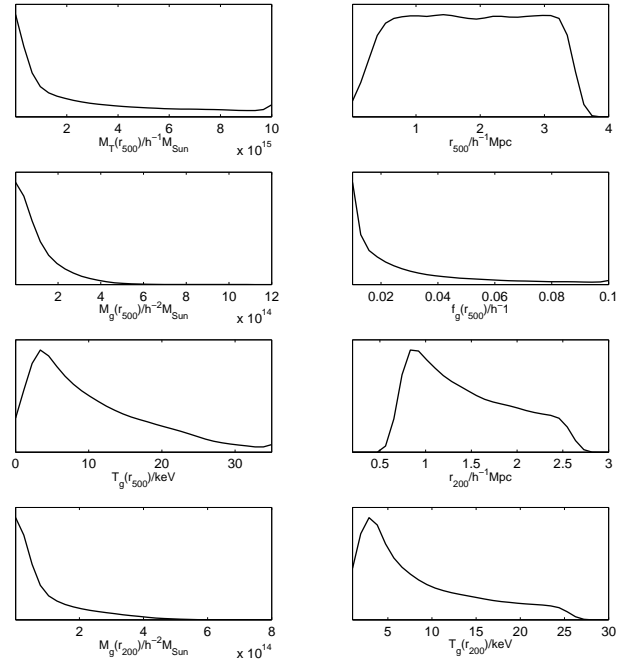


Figure 16. Marginal distributions of the derived cluster physical parameters with no data for "entropy"-GNFW pressure model.

the isothermal β -model observed with the AMI SA and used these simulated data to study three different parameterisations in deriving the cluster physical parameters. We showed that in generating AMI simulated data, it is extremely important to select the model parameters describing the SZ signal in a way that leads to the consistent cluster parameter inferences upon using the three different parameterisation methods.

We found that each parameterisation introduces different constraints and biases in the posterior probability distribution of the inferred cluster parameters which arise from the way we imple-

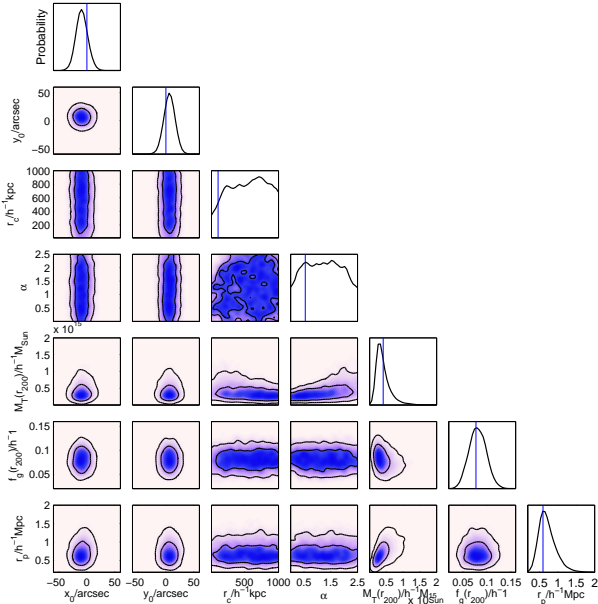


Figure 17. Marginal distributions of the sampling parameters with simulated data for “entropy”-GNFW pressure model using parameterisation II.

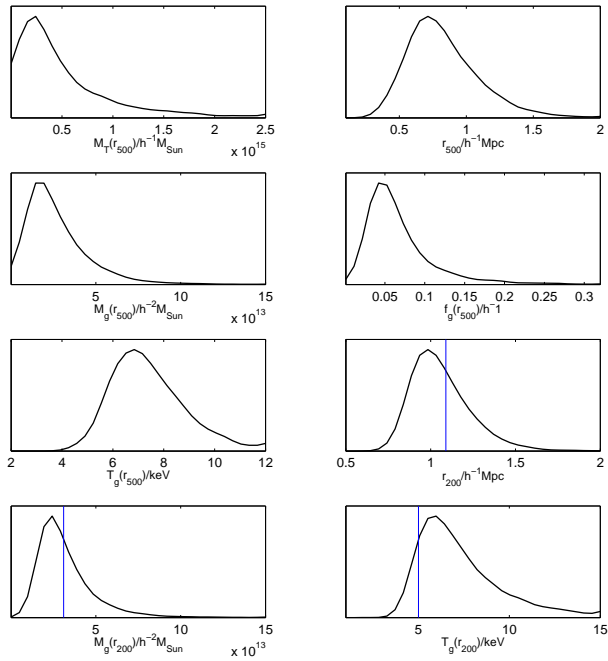


Figure 18. Marginal distributions of the derived cluster physical parameters with simulated data for “entropy”-GNFW pressure model using parameterisation II.

ment assumptions about the cluster structure and its composition. The biases in the posterior probability distributions of the cluster parameters are more pronounced in parameterisations I and II, as the results depend strongly on the relatively unconstrained cluster model shape parameters: r_c and β . However, the biases introduced by the choice of priors are even worse in parameterisation I, in which the gas temperature is assumed to be an independent free parameter. This, along with the assumption of isothermality, causes the priors to dominate in extracting the cluster physical parameters regardless the type of prior chosen for the gas tempera-

Table 11. Simulated cluster parameters estimated (mean, standard deviation and Maximum likelihood) using “entropy”-GNFW pressure model– parameterisation II assuming $h = 0.7$.

Parameter	$\mu \pm \sigma$	$\hat{\mu}$
x_c	$-8.9 \pm 10.04''$	$-9.3''$
y_c	$6.3 \pm 9.5''$	$7.8''$
r_c	770.43 ± 382.29 kpc	1358.86 kpc
α	1.2 ± 0.67	1.2
$M_T(r_{200})$	$(5.86 \times 10^{14} \pm 3.43 \times 10^{14}) M_\odot$	$3.3 \times 10^{14} M_\odot$
$f_g(r_{200})$	0.11 ± 0.02	0.13
r_p	1.03 ± 0.33 Mpc	0.87 Mpc
$M_T(r_{500})$	$(8.86 \pm 11.57) \times 10^{14} M_\odot$	$4.0 \times 10^{14} M_\odot$
r_{500}	1.18 ± 0.39 Mpc	1.01 Mpc
$M_g(r_{500})$	$(5.71 \pm 4.08) \times 10^{13} M_\odot$	$3.06 \times 10^{13} M_\odot$
$f_g(r_{500})$	0.1 ± 0.09	0.07
$T_g(r_{500})$	7.5 ± 1.8 keV	6.5 keV
r_{200}	1.57 ± 0.28 Mpc	1.3 Mpc
$M_g(r_{200})$	$(6.53 \pm 3.67) \times 10^{13} M_\odot$	$4.14 \times 10^{13} M_\odot$
$T_g(r_{200})$	7.4 ± 2.6 keV	5.02 keV

Table 12. Simulated cluster parameters estimated (mean, standard deviation and Maximum likelihood) using entropy-GNFW pressure model– parameterisation III assuming $h = 0.7$.

Parameter	$\mu \pm \sigma$	$\hat{\mu}$
x_c	$-8.8 \pm 9.8''$	$-10.4''$
y_c	$6.6 \pm 9.5''$	$7.2''$
r_c	798.7 ± 376.8 kpc	1280.8 kpc
α	1.3 ± 0.69	1.3
$M_T(r_{200})$	$(8.0 \times 10^{14} \pm 5.6 \times 10^{14}) M_\odot$	$4.5 \times 10^{14} M_\odot$
$f_g(r_{200})$	0.11 ± 0.03	0.13
r_p	1.0 ± 0.3 Mpc	0.86 Mpc
$M_T(r_{500})$	$(6.6 \pm 1.14) \times 10^{14} M_\odot$	$3.4 \times 10^{14} M_\odot$
r_{500}	1.14 ± 0.43 Mpc	1.0 Mpc
$M_g(r_{500})$	$(7.35 \pm 5.92) \times 10^{13} M_\odot$	$3.67 \times 10^{13} M_\odot$
$f_g(r_{500})$	0.14 ± 0.14	0.11
$T_g(r_{500})$	6.0 ± 1.4 keV	5.5 keV
r_{200}	1.7 ± 0.28 Mpc	1.4 Mpc
$M_g(r_{200})$	$(9.18 \pm 5.71) \times 10^{13} M_\odot$	$5.91 \times 10^{13} M_\odot$
$T_g(r_{200})$	5.98 ± 2.43 keV	4.2 keV

ture (AMI Consortium: Rodríguez-González et al. 2011 and AMI Consortium: Zwart et al. 2010). The cluster physical parameters estimated using parameterisation I depend strongly on the model parameters. Although it can constrain the cluster position and its $M_g(r_{200})$, it fails to recover the true input values of most of the simulated cluster properties. For example the inferred values for mass and temperature at r_{200} are $M_T(r_{200}) = (6.43 \pm 5.43) \times 10^{15} M_\odot$ and $T_g(r_{200}) = (10.61 \pm 5.28)$ keV whereas the corresponding input values of simulated cluster are: $M_T(r_{200}) = 5.83 \times 10^{14} M_\odot$ and $T_g(r_{200}) = 5$ keV. In terms of the application to the real data, we have noticed similar biases in the results of our analysis of 7 clusters using this parameterisation (AMI Consortium: Zwart et al. 2010). In order to improve our analysis methodology in parameterisations II and III, the correlation between the cluster total mass and its gas temperature is taken into account. In parameterisation II we relate $M_T(r_{200})$ and $T_g(r_{200})$ using the hydrostatic equilibrium whereas in parameterisation III we use virial mass-temperature relationship. It should be noted that the derived $T_g(r_{200})$ in parameterisation II is the gas temperature at the overdensity radius r_{200} which is then assumed to be constant throughout the cluster. In parameter-

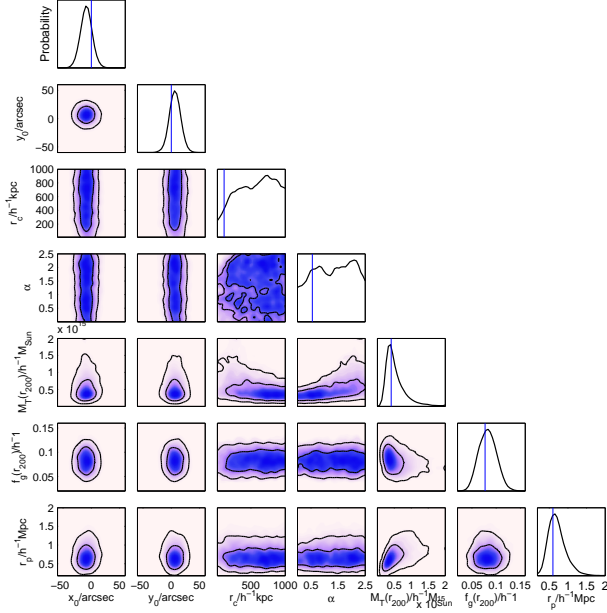


Figure 19. Marginal distributions of the sampling parameters with simulated data for "entropy"-GNFW pressure model using parameterisation III.

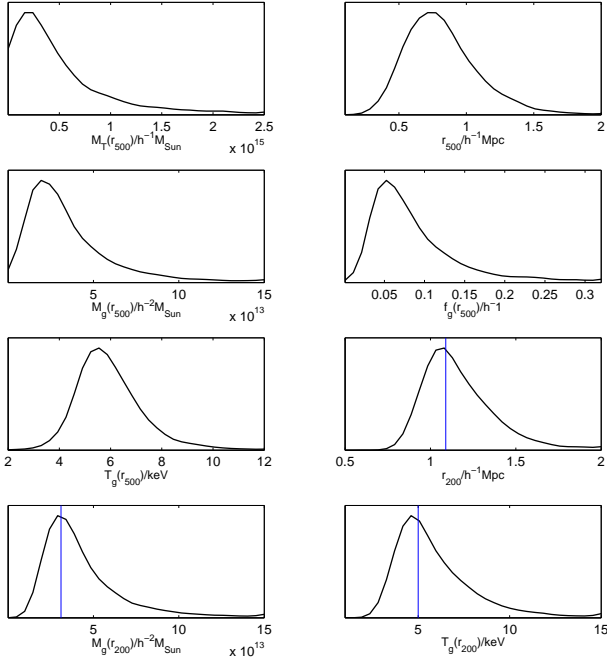


Figure 20. Marginal distributions of the derived cluster physical parameters with simulated data for "entropy"-GNFW pressure model using parameterisation III.

isation III, however, $T_g(r_{200})$ is the mean gas temperature internal to radius r_{200} and is assumed to be constant. We notice that analysing the same simulated data set using parameterisation II can constrain the 1-D posterior distribution of the cluster physical parameters better than parameterisation I such that $M_T(r_{200}) = (6.8 \pm 2.1) \times 10^{14} M_\odot$ and $T_g(r_{200}) = (3.0 \pm 1.2) \text{ keV}$. Since parameterisation II uses the full parametric hydrostatic equilibrium, the temperature estimate depends on r_c and β and is therefore biased low. These results were also confirmed in our analysis of the bullet like cluster A2146 (AMI Consortium: Rodríguez-González et al. 2011). Relating the cluster

Table 13. The results of 100 CMB realisations for the three parameterisations assuming $h=0.7$.

parameterisation	$M_T(r_{200}) M_\odot$	$T_g(r_{200}) \text{ keV}$
I	$(6.18 \pm 5.23) \times 10^{15}$	11.18 ± 5.16
II	$(8.067 \pm 2.61) \times 10^{14}$	3.94 ± 1.67
III	$(5.94 \pm 2.26) \times 10^{14}$	4.97 ± 1.21

total mass and its temperature via virial theorem in parameterisation III leads to less bias in cluster physical parameters compared to the other two parameterisations as it is less model dependent: $M_T(r_{200}) = (4.68 \pm 1.56) \times 10^{14} M_\odot$ and $T_g(r_{200}) = (4.3 \pm 0.9) \text{ keV}$.

A detailed comparison between our different parameterisations both using simulated data and on the bullet like cluster A2146 (AMI Consortium: Rodríguez-González et al. 2011) found that parameterisation III can give more reliable results for cluster physical properties as it is less dependent on model parameters. Parameterisation II also gives convincing estimates for the cluster total mass and its gas content although its temperature estimate is poorly justified, as it depends strongly on the model parameters. Moreover, young or disturbed clusters are unlikely to be well-described by hydrostatic equilibrium. We therefore used parameterisation III as our adopted analysis methodology in our follow-up studies of the real clusters including the joint SZ and weak lensing analysis of six clusters (AMI Consortium: Hurley-Walker et al. 2011) and the analysis of LoCuss cluster sample (AMI Consortium: Rodríguez-González et al. 2011; AMI Consortium: Shimwell et al. 2011).

In order to make sure that our results are not biased by one realisation of primordial CMB, we have studied 100 CMB realisations for the three parameterisations. The 1-D marginalised posterior probability distributions of $M_T(r_{200})$ and $T_g(r_{200})$ are shown in Figs. 21, 22 and 23 for each parameterisation. The solid blue line represents the true value corresponding to the simulated cluster and the dashed red line shows the mean value of the distributions. Table 13 also presents the numerical results of this analysis. Comparing the 1D posterior distributions along with the mean values of the $M_T(r_{200})$ estimates in the three parameterisations for these 100 realisations show that parameterisation I can hardly constrain the simulated cluster properties and recover the input true values. Parameterisation II can constrain the cluster total mass, however, the gas temperature estimate is biased low as it depends on unconstrained model shape parameters. On the other hand, parameterisation III can indeed constrain both cluster mass and its gas temperature and the results are unbiased.

In order to remove the assumption of isothermality which is of course a poor assumption both within the cluster inner region and at the large radii and to improve our analysis model for the cluster ICM which can be fitted accurately throughout the cluster, we also studied the SZ effect using "entropy"-GNFW pressure model. This model assumes a 3-D β -model like radial profile describing the entropy in the ICM as well as the GNFW profile for the plasma pressure. This choice is reasonable as the entropy is a conserved quantity and describes the structure of the ICM while the pressure is related to the dark matter component of the cluster. Moreover, among all the thermodynamical quantities describing the ICM, entropy and pressure show more self-similar distribution in the outskirts of the cluster. The combination of these two profiles then allows us to relate the SZ observable properties to the cluster physical parameters such as its total mass. This model also allows the electron pressure and its number density profiles to have different

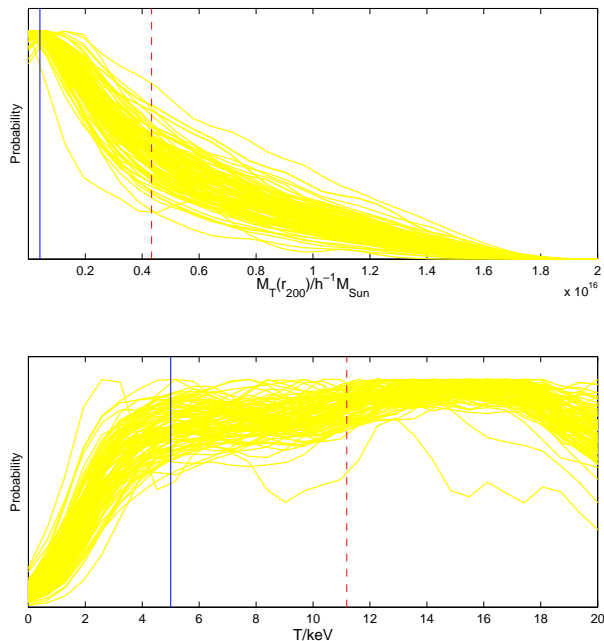


Figure 21. 100 realisations of 1-D marginalised posterior probability distributions of $M_T(r_{200})$ and $T_g(r_{200})$ using isothermal β -model–parameterisation I. The solid blue line represents the true value corresponding to the simulated cluster and the dashed red line shows the mean value of the distributions.

distributions leading to a 3-D radial temperature profile. In this context we simulated a second cluster using an entropy-GNFW pressure profile with the same physical parameters and thermal noise as the first cluster at r_{200} .

We then analysed the second simulated cluster using “entropy”-GNFW pressure model with different parameterisations. In this model temperature is no longer isothermal so that we can not use parameterisation I where a single temperature is assumed as an independent input parameter. The results of our analysis using parameterisation II and III show that while the characteristic scaling radius describing the GNFW pressure profile is constrained, the shape parameters defining the entropy profile remain unconstrained. Moreover, all the cluster physical parameters lie within 1σ errorbars from the corresponding true values of the simulated cluster in the two parameterisations. However, parameterisation III provides tighter constrains in 1-D marginalised posterior distribution of the temperature and the overall results are less model dependent so that it can be reliably used in the analysis of galaxy clusters in particular when the assumption of hydrostatic equilibrium breaks (e.g. in disturbed clusters and clusters that are going through merging).

We conclude that using the “entropy”-GNFW pressure model overcomes the limitations of the isothermal β -model in fitting cluster parameters over a broad radial extent. However, AMI simulated data do not strongly prefer one model over the other. We investigated this conclusion further by fitting both GNFW pressure profile and isothermal β -model to a simulated cluster with $\theta_{500} = 2.5'$ and $Y_{500} = 2.5 \times 10^{-3} (\text{arcmin})^2$. The result is shown in Fig. 24 with blue dashed line representing the fit using the isothermal β -model and the red representing the fit using GNFW pressure profile. However, we aim to compare these two models in our future studies using the real data.

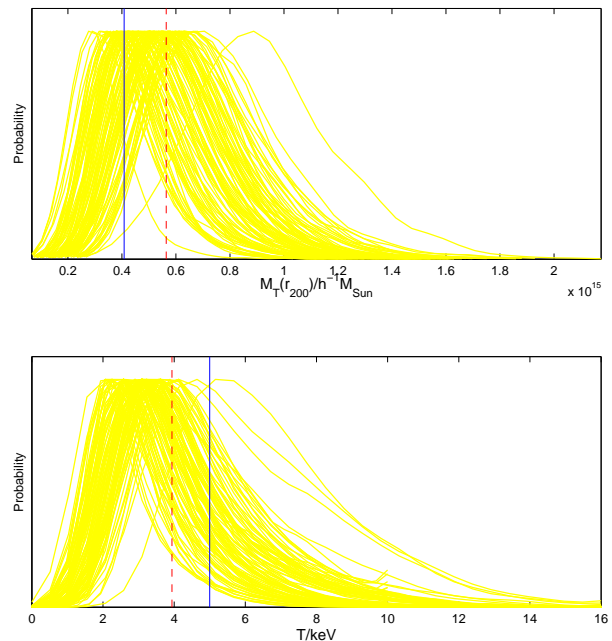


Figure 22. 100 realisations of 1-D marginalised posterior probability distributions of $M_T(r_{200})$ and $T_g(r_{200})$ using isothermal β -model–parameterisation II. The solid blue line represents the true value corresponding to the simulated cluster and the dashed red line shows the mean value of the distributions.

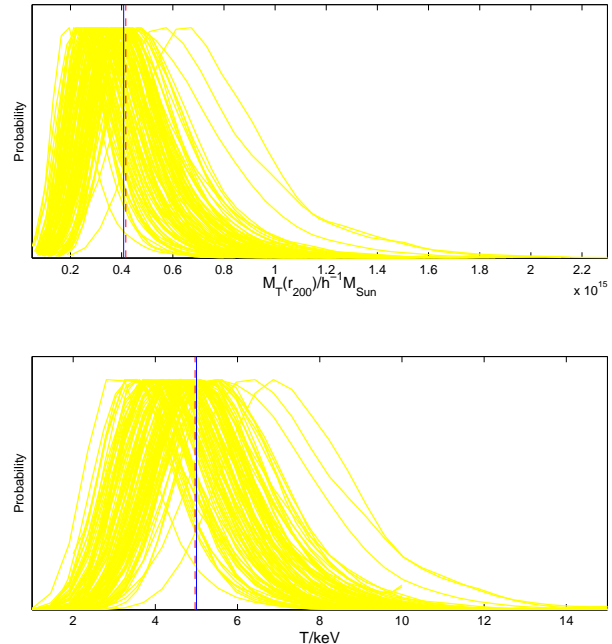


Figure 23. 100 realisations of 1-D marginalised posterior probability distributions of $M_T(r_{200})$ and $T_g(r_{200})$ using isothermal β -model–parameterisation III. The solid blue line represents the true value corresponding to the simulated cluster and the dashed red line shows the mean value of the distributions.

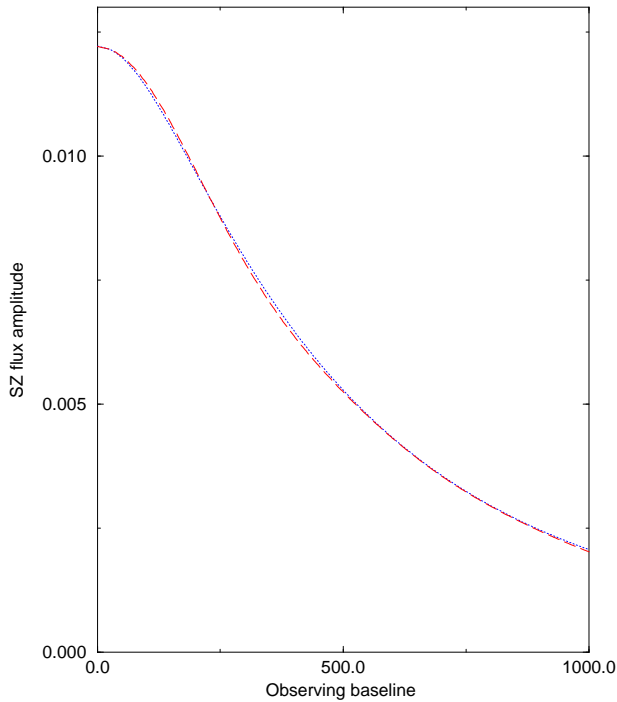


Figure 24. The SZ flux amplitude versus AMI SA observing baseline for a cluster with $\theta_{500} = 2.5'$ and $Y_{500} = 2.5 \times 10^{-3}(\text{arcmin})^2$. Blue dashed line represents the fit using the isothermal β -model and the red represents the fit using GNFw pressure profile.

ACKNOWLEDGMENTS

The analysis work was conducted on the Darwin Supercomputer of the University of Cambridge High Performance Computing Service supported by HECCE. The authors thank Stuart Rankin for computing assistance. We also thank Dave Green for his invaluable help with L^AT_EX. MO, CRG, MLD, TMOF, MPS and TWS acknowledge PPARC/STFC studentships.

REFERENCES

- Afshordi N., Cen R., 2002, *ApJ*, 564, 669
 Afshordi N., Lin Y.-T., Nagai D., Sanderson A. J. R., 2007, *MNRAS*, 378, 293
 Allison J. R., Taylor A. C., Jones M. E., Rawlings S., Kay S. T., 2011, *MNRAS*, 410, 341
 AMI Consortium: Hurley-Walker N. et al., 2011, arXiv:1101.5912
 AMI Consortium: Rodríguez-González C. et al., 2011, *MNRAS*, 661
 AMI Consortium: Rodríguez-González C. et al., 2011, arXiv:1101.5589
 AMI Consortium: Shimwell T. et al., 2010, arXiv:1012.4441
 AMI Consortium: Shimwell T. et al., 2011, arXiv:1101.5590
 AMI Consortium: Zwart J. T. L., et al., 2008, *MNRAS*, 391, 1545
 AMI Consortium: Zwart J. T. L., et al., 2011, *MNRAS*, 1931
 Andersson K., et al., 2011, *ApJ*, 738, 48
 Arnaud M., Pointecouteau E., Pratt G. W., 2005, *A&A*, 441, 893
 Arnaud M., Pratt G. W., Piffaretti R., Böhringer H., Croston J. H., Pointecouteau E., 2010, *A&A*, 517, A92
 Bartlett J. G., Silk J., 1994, *ApJ*, 423, 12
 Bautz M. W., et al., 2009, *PASJ*, 61, 1117
 Birkinshaw M., 1999, *PhR*, 310, 97
 Böhringer H. et al., 2007, *A&A*, 469, 363
 Borgani S., et al., 2004, *MNRAS*, 348, 1078
 Borgani S., 2004, *Ap&SS*, 294, 51
 Carlstrom J. E., Holder G. P., Reese E. D., 2002, *ARA&A*, 40, 643
 Cavaliere A., Fusco-Femiano R., 1976, *A&A*, 49, 137
 Cavaliere A., Fusco-Femiano R., 1978, *A&A*, 70, 677
 Challinor A., Lasenby A., 1998, *ApJ*, 499, 1
 da Silva A. C., Kay S. T., Liddle A. R., Thomas P. A., 2004, *MNRAS*, 348, 1401
 Eke V. R., Cole S., Frenk C. S., Patrick Henry J., 1998, *MNRAS*, 298, 1145
 Eke V. R., Navarro J. F., Frenk C. S., 1998, *ApJ*, 503, 569
 Ettori S., Morandi A., Tozzi P., Balestra I., Borgani S., Rosati P., Lovisari L., Terenziani F., 2009, *A&A*, 501, 61
 Evrard A. E., Metzler C. A., Navarro J. F., 1996, *ApJ*, 469, 494
 Evrard A. E., et al., 2002, *ApJ*, 573, 7
 Feroz F., Hobson M. P., 2008, *MNRAS*, 384, 449
 Feroz F., Hobson M. P., Bridges M., 2009, *MNRAS*, 398, 1601
 Feroz F., Hobson M. P., Zwart J. T. L., Saunders R. D. E., Grainge K. J. B., 2009, *MNRAS*, 398, 2049
 Finoguenov A., Reiprich T. H., Böhringer H., 2001, *A&A*, 368, 749
 Finoguenov A., 2002, *ASPC*, 253, 71
 Fixsen D. J., Cheng E. S., Gales J. M., Mather J. C., Shafer R. A., Wright E. L., 1996, *ApJ*, 473, 576
 George M. R., Fabian A. C., Sanders J. S., Young A. J., Russell H. R., 2009, *MNRAS*, 395, 657
 Grainge K., Jones M. E., Pooley G., Saunders R., Edge A., Grainger W. F., Kneissl R., 2002, *MNRAS*, 333, 318
 Grego L., Carlstrom J. E., Reese E. D., Holder G. P., Holzapfel W. L., Joy M. K., Mohr J. J., Patel S., 2001, *ApJ*, 552, 2
 Hallman E. J., Burns J. O., Motl P. M., Norman M. L., 2007, *ApJ*, 665, 911
 Hobson M. P., Maisinger K., 2002, *MNRAS*, 334, 569
 Hoshino A., et al., 2010, *PASJ*, 62, 371
 Kawaharada M., et al., 2010, *ApJ*, 714, 423
 Itoh N., Kohyama Y., Nozawa S., 1998, *ApJ*, 502, 7
 Jones M., et al., 1993, *Natur*, 365, 320
 Kaiser N., 1986, *MNRAS*, 222, 323
 Komatsu E., et al., 2011, *ApJS*, 192, 18
 Kravtsov A. V., Gnedin O. Y., 2005, *ApJ*, 623, 650
 Kravtsov A. V., Nagai D., Vikhlinin A. A., 2005, *ApJ*, 625, 588
 Kravtsov A. V., Vikhlinin A., Nagai D., 2006, *ApJ*, 650, 128
 Larson D., et al., 2011, *ApJS*, 192, 16
 Lewis A., Challinor A., Lasenby A., 2000, *ApJ*, 538, 473
 Lloyd-Davies E. J., Ponman T. J., Cannon D. B., 2000, *MNRAS*, 315, 689
 Mason B. S., Myers S. T., 2000, *ApJ*, 540, 614
 Maughan B. J., 2007, *ApJ*, 668, 772
 Maughan B. J., Jones C., Jones L. R., Van Speybroeck L., 2007, *ApJ*, 659, 1125
 McCarthy I. G., Bower R. G., Balogh M. L., 2007, *MNRAS*, 377, 1457
 Mitchell N. L., McCarthy I. G., Bower R. G., Theuns T., Crain R. A., 2009, *MNRAS*, 395, 180
 Mroczkowski T., et al., 2009, *ApJ*, 694, 1034
 Nagai D., 2006, *ApJ*, 650, 538
 Nagai D., Kravtsov A. V., Vikhlinin A., 2007, *ApJ*, 668, 1
 Nagai D., Lau E. T., 2011, *ApJ*, L10
 Nagai D., 2011, *MmSAI*, 82, 594
 Nozawa S., Itoh N., Kohyama Y., 1998, *ApJ*, 508, 17
 Piffaretti R., Valdarnini R., 2008, *A&A*, 491, 71
 Plagge T., et al., 2010, *ApJ*, 716, 1118

- Planck Collaboration, et al., 2011, *A&A*, 536, A12
- Planck Collaboration, et al., 2011, *A&A*, 536, A11
- Planck Collaboration, et al., 2011, *A&A*, 536, A10
- Planck Collaboration, et al., 2011, *A&A*, 536, A9
- Planck Collaboration, et al., 2011, *A&A*, 536, A8
- Pointecouteau E., Giard M., Barret D., 1998, *A&A*, 336, 44
- Pointecouteau E., Arnaud M., Pratt G. W., 2005, *A&A*, 435, 1
- Ponman T. J., Cannon D. B., Navarro J. F., 1999, *Nature*, 397, 135
- Ponman T. J., Sanderson A. J. R., Finoguenov A., 2003, *MNRAS*, 343, 331
- Pratt G. W., Arnaud M., 2002, *A&A*, 394, 375
- Pratt G. W., Arnaud M., Pointecouteau E., 2006, *A&A*, 446, 429
- Pratt G. W., Arnaud M., Pointecouteau E., 2006, *ESASP*, 604, 695
- Pratt G. W., et al., 2010, *A&A*, 511, A85
- Press W. H., Schechter P., 1974, *ApJ*, 187, 425
- Reiprich T. H., et al., 2009, *A&A*, 501, 899
- Rephaeli Y., 1995, *ARA&A*, 33, 541
- Sanderson A. J. R., Ponman T. J., 2003, *MNRAS*, 345, 1241
- Sanderson A. J. R., Ponman T. J., Finoguenov A., Lloyd-Davies E. J., Markevitch M., 2003, *MNRAS*, 340, 989
- Sarazin C. L., 1988, *X-ray Emission from Clusters of Galaxies*, Cambridge University Press
- Sarazin C. L., 2008, *LNP*, 740, 1
- Simionescu A., et al., 2011, *Sci*, 331, 1576
- Skilling J., 2004, *AIP Conf. Proc.*, 735, 395
- Sunyaev R. A., Zeldovich Y. B., 1970, *CoASP*, 2, 66
- Tozzi P., Norman C., 2001, *ApJ*, 546, 63
- Urban O., Werner N., Simionescu A., Allen S. W., Böhringer H., 2011, *MNRAS*, 414, 2101
- Vikhlinin A., Markevitch M., Murray S. S., Jones C., Forman W., Van Speybroeck L., 2005, *ApJ*, 628, 655
- Vikhlinin A., Kravtsov A., Forman W., Jones C., Markevitch M., Murray S. S., Van Speybroeck L., 2006, *ApJ*, 640, 691
- Voit G. M., 2000, *ApJ*, 543, 113
- Voit G. M., Ponman T. J., 2003, *ApJ*, 594, L75
- Voit G. M., 2004, *IAU Colloq. 195: Outskirts of Galaxy Clusters: Intense Life in the Suburbs*, *ogci.conf*, 253
- Voit G. M., 2005, *RvMP*, 77, 207
- Wadsley J. W., Veeravalli G., Couchman H. M. P., 2008, *MNRAS*, 387, 427
- Yoshikawa K., Jing Y. P., Suto Y., 2000, *ApJ*, 535, 593